An Experimental Investigation into the Wildland Fire Burning Characteristics of Loblolly Pine Straw

by

Daniel C. Stubbs

A thesis submitted to the Graduate Faculty of
Auburn University
in partial fulfillment of the
requirements for the Degree of
Master of Science

Auburn, Alabama
August 7, 2021

Keywords: wildland fires, loblolly pine straw, optical diagnostics, experimental analysis, CH* chemiluminescence

Approved by

David Scarborough, Assistant Professor of Aerospace Engineering
Vrishank Raghav, Assistant Professor of Aerospace Engineering
Brian Thurow, Department Chair, W. Allen and Martha Reed Professor

Abstract

Wildland fires present a threat to both the environment and to homes and businesses in the wildland urban interface. Understanding the behavior of wildland fires is crucial for developing informed risk management techniques, such as prescribed burning, to prevent uncontrolled fires, which devastate communities globally. In this work, an optically accessible facility was developed combining traditional and optical diagnostic techniques to study the combustion of wildland fuels. The developed testing facility was then used to measure the burning characteristics of loblolly pine (*Pinus taeda*) straw. Mass loss rate, flame temperature, propagation rate, flame geometry, chemiluminescent flame intensity, and pollutant emissions from the fire were measured for fuel loadings of 0.98, 1.31, and 1.63 $\mathrm{kg/m^2}$. Mass loss rate was found to increase with fuel loading. The flame propagation rate was found to increase slightly while approaching an asymptotic value. The flame height increased more significantly with fuel loading, but also approached an asymptotic value. Flame length was found to increase slightly with fuel loading, and throughout the duration of the test. Flame surface area was found to increase linearly with fuel loading, indicating that the flame length may be increasing in a way that compensates for the asymptotic nature of the flame height. The flame intensity and flame temperatures did not change significantly, suggesting they are driven by the chemical kinetics of the pine straw combustion rather than the physical arrangement of the fuel bed. Carbon monoxide emissions were found to increase significantly with fuel loading, while sulfur dioxide increased only slightly, and nitrogen oxides remained near zero. It was concluded that most mass loss is due to flaming combustion in the leading flame front. The results presented here can be used to inform prescribed burning practices to reduce the risk of uncontrolled fire, manage ecosystem health, and as useful validation data for wildland fire modeling codes currently under development.

Acknowledgments

I would like to thank all of my family and friends who have helped me along the way. Thank you for your advice, encouragement, and support throughout this process.

To my Mom and Dad, thank you for always encouraging me to pursue my dreams and for your unwavering support on whatever path I chose.

To my girlfriend of seven years, Kayla, thank you for always being there for me, listening to my endless complaining about work, and tolerating the long hours that graduate school sometimes requires.

To my advisor Dr. David Scarborough, thank you for your leadership and advice throughout this process. You have helped me grow into the researcher that I am today, and without you this work would not have been possible.

Lastly, I would like to thank Austin Childtree, Luke Humphreys, Eric Van Horn, Ari Goldman, and all other members of the Auburn University Combustion Physics Lab, both past and present, who have contributed to this work both physically and intellectually.

This work was funded by the Auburn University Intramural Grants Program.

Table of Contents

Abstract ii

Acknowledgments iii

List of Abbreviations x

1 Introduction 1

2 Previous Work 3

2.1 Chemical Kinetics Studies 3

2.2 Macroscopic Fire Property Studies 4

2.2.1 Slope Effects 7

2.2.2 Wind Effects 11

2.2.3 Fuel Moisture Content 13

3 Experimental Methods 14

3.1 The Wildland Fire Integrated Research Experiment 14

3.2 Data Acquisition 17

3.3 Data Processing 18

3.4 Mass Consumption Measurements 20

3.5 Temperature Measurements 21

3.6 Emissions Measurements 23

3.7 Optical Diagnostics 24
3.7.1 Flame Intensity Measurements 26
3.7.2 Flame Propagation Measurements 27
3.7.3 Flame Length Measurements 29
3.7.4 Flame Height Measurements 29
3.7.5 Camera Calibration 30

4 Results and Discussion 33
4.1 Mass Consumption Rate 33
4.2 Temperatures 39
4.3 Optical Diagnostic Results 45
4.3.1 Flame Front Propagation Rate 46
4.3.2 Flame Height 52
4.3.3 Flame Length 55
4.3.4 Flame Area 57
4.3.5 Flame Intensity 60
4.4 Emissions 62
4.5 Comparison with previous results 66

5 Conclusions 71

References 76

List of Figures

3.1 Computer Graphics Rendering of the WildFIRE Facility. The load cells and weight plate are highlighted in red and blue, respectively. 15

3.2 The LabVIEW control panel for the WildFIRE data acquisition program. 18

3.3 Diagram showing the locations of each thermocouple within the WildFIRE facility. 22

3.4 An example figure depicting how the flame detection processing works. Frame (a) shows the cropped monochrome flame image. Frames (b), (c), and (d) all show the resulting thresholded image along with the points identified on the rear, forward, and top edge of the flame, respectively. The red lines represent the location of the frame rear (b), flame front (c), and flame height (d). 26

3.5 Shows an example of an outlier point (circled in red) being undesirably identified as flame. 28

3.6 An example of one of the checkerboard calibration images taken to calibrate the flame geometry distance measurements. 31

4.1 Time history of fuel mass for a range of initial fuel loadings. The solid line and shaded region represent the mean and 95% confidence interval, respectively, across ten tests at each fuel loading. The vertical dashed lines denote the steady-state region. 34

4.2 Time history of normalized fuel mass for a range of initial fuel loadings. The solid line and and shaded region represent the mean and 95% confidence interval, respectively, across ten tests at each fuel loading. 35

4.3 Mean burn rate versus initial fuel loading for a range of fuel loadings. Error bars denote the 95% confidence interval. 36

4.4 Mean residual mass fraction for a range of initial fuel loadings. Error bars denote the 95% confidence interval. 38

4.5 Time history of the flame temperature as measured by the bottom thermocouple in the middle column of thermocouples. The mean value averaged across the tests at each fuel loading is shown via the solid line and the 95% confidence interval is represented by the shaded region. 40

4.6 Time history of the flame temperature as measured by the middle thermocouple in the middle column of thermocouples. The mean value averaged across the tests at each fuel loading is shown via the solid line and the 95% confidence interval is represented by the shaded region. 41

4.7 Time history of the flame temperature as measured by the top thermocouple in the middle column of thermocouples. The mean value averaged across the tests at each fuel loading is shown via the solid line and the 95% confidence interval is represented by the shaded region. 42

4.8 Maximum flame temperature as a function of relative location within the flame height for the range of initial fuel loadings. Error bars denote the 95% confidence interval. 43

4.9 Optically tracked flame front for a range of initial fuel loadings. The solid line and shaded region represent the mean and 95% confidence interval, respectively, across ten tests at each fuel loading. 46

4.10 Propagation rate of the flame front as calculated from the optically tracked flame fronts for a range of initial fuel loadings. Error bars denote the 95% confidence interval. 47

4.11 Comparison of the mass loss rate measured using load cells with the mass loss rate calculated from the optically tracked flame front propagation. The error bars denote the 95% confidence interval. 50

4.12 Comparison of the propagation rate measured from the optically tracked flame front compared with the propagation rate calculated from the mass loss data. The error bars denote the 95% confidence interval. 52

4.13 Flame height versus time for a range of initial fuel loadings. The solid line and shaded region represent the mean and 95% confidence interval, respectively, across ten tests at each fuel loading. The dashed lines denote the steady-state region. . . . 53

4.14 Mean flame height for a range of initial fuel loadings. Error bars denote the 95% confidence interval. 54

4.15 Flame length versus time for a range of initial fuel loadings. The solid line represents the mean across three tests at each fuel loading and the shaded region represents the 95% confidence interval. 56

4.16 Flame area versus time for a range of initial fuel loadings. The solid line represents the mean across three tests at each fuel loading and the shaded region represents the 95% confidence interval. 58

4.17 Flame area for a range of initial fuel loadings. Error bars denote the 95% confidence interval. 59

4.18 Normalized Flame intensity for a range of initial fuel loadings. The solid line and shaded region represent the mean and 95% confidence interval, respectively, across ten tests at each fuel loading. 60

4.19 Flame intensity for a range of initial fuel loadings. Error bars denote the 95% confidence interval. 61

4.20 Relative average CO output for a range of initial fuel loadings. Error bars denote the standard error of the mean. 63

4.21 Relative average NOx output for a range of initial fuel loadings. Error bars denote the standard error of the mean. 64

4.22 Relative average SO_2 output for a range of initial fuel loadings. Error bars denote the standard error of the mean. 65

4.23 Comparison of the mass loss rate measured in the present study to mass loss rate measured from a few similar studies. 68

4.24 Comparison of the flame propagation rate in the present study to flame propagation rate measured from a few similar studies. 68

List of Tables

3.1 Fuel bed thickness for each initial fuel loading value tested. The experimental variation in actual fuel loading values compared to the target value is also listed. . . 16

4.1 Table of results from mass loss data. The 95% confidence interval is shown in parenthesis. 37

4.2 Maximum flame temperature at each height for the three initial fuel loadings tested. The 95% confidence interval is shown in parenthesis. 44

4.3 Relative thermocouple locations reported as fraction of total flame height. Negative values indicate that the thermocouple is located in the fuel bed, beneath the bottom of the flaming combustion zone. 44

4.4 Table of optically tracked fire propagation rate results. The 95% confidence interval is shown in parenthesis. 48

4.5 Table of optically tracked flame height results. The 95% confidence interval is shown in parenthesis. 55

4.6 Table of flame surface area results. The 95% confidence interval is shown in parenthesis. 59

4.7 Table of chemiluminescent flame intensity results. The 95% confidence interval is shown in parenthesis. 62

4.8 Table of pollutant species concentrations. The standard error is shown in parenthesis. 66

List of Abbreviations

χ	Pollutant concentration
$\dot{L}_{\mathrm{meas}}$	Propagation rate measured from the optically tracked flame front
$\dot{m}_{\mathrm{calc}}$	Mass loss rate calculated from the propagation rate
$\dot{m}_{\mathrm{meas}}$	Mass loss rate measured directly from the mass loss data
η	Residual mass fraction
η_i	Residual mass fraction
$\mathrm{SE}(t)$	Standard error of the mean as a function of time
$\mu(t)$	Mean as a function of time
$\overline{\chi}$	Mean pollutant concentration
$\overline{\dot{L}}$	Mean propagation rate
$\overline{\dot{m}}$	Mean burn rate
$\overline{A}$	Mean flame surface area
$\overline{H}$	Mean flame height
$\overline{I}$	Mean intensity

$\overline{W}$	Mean flame length
$\overline{X}_{\mathrm{FL}}$	Mean burning characteristic for a given fuel loading
ρ	Bulk density of the fuel
$\sigma(t)$	Standard deviation as a function of time
$\tau_{i,j,k}(t)$	Time history of thermocouple k in row j during test i
A	Flame surface area
A_{CS}	Width-wise cross-sectional area of the fuel bed
bd	The bit depth of the flame images
H	Flame height
H_{FB}	Height of the fuel bed
I	Flame intensity
$I_i(t)$	chemiluminescence intensity of the flame as a function of time for test i
$I_p(t)$	The intensity of each flame pixel
$I_{p,\max}$	The maximum possible intensity of each pixel
j	Thermocouple row index
L	Flame front location
L_{FB}	Length of the fuel bed
m	Fuel mass
m_b	Mass of fuel burned

m_f	Final fuel mass
m_o	Initial fuel mass
n_f	The number of flame pixels in a given image
n_s	Number of tests at each fuel loading
T	Temperature
t_f	Final time
t_o	Initial time
t_s	t-value
W	Flame length
W_{FB}	Width of the fuel bed
X	Stand-in used to represent any one of the multiple burning characteristics studied
$X_i(t)$	Recorded burning characteristic as a function of time
CI	95% confidence interval
FL	Fuel loading
i	Test index
t	Time

Chapter 1

Introduction

Wildfires affect not only the United States, but the entire global community [1–4]. Wildfire was once a frequently occurring, natural disturbance initiated most commonly by lightning in numerous ecologically important environments. However, across much of the modern landscape the fire process has been significantly altered and sometimes eliminated through human intervention. In the absence of fire, leaves, needles, and small sticks accumulate on the forest floor over the period of many years. Furthermore, many woody species such as wax myrtle and yaupon holly grow uncontrolled under the tree canopy. Therefore when fire does finally occur, as it most assuredly will, it is exacerbated by many years' worth of accumulated fuel and woody plants propagating rapidly with high heat intensity and tall flames.

Prescribed, or controlled, burning is a type of intervention that seeks to provide the benefits of natural wildland fires while minimizing the potential threats to property and other anthropogenic concerns. These prescribed burns, when repeated at frequent intervals, serve to consume the fuel materials on the forest floor thereby reducing the risk of an uncontained fire. Although prescribed fire reduces the risk of damaging wildfire and promotes forest restoration and wildlife habitat, significant regulatory and public perception hurdles to the use of prescribed fire exist. The primary reason is that data on wildfire and prescribed burns are difficult to obtain due to the cost and risks posed from fire on the scale which wildland fires occur. On the opposite end of the spectrum, small-scale laboratory studies fail to include many relevant factors. Therefore, a need exists for an

intermediate-scale facility designed to obtain data on the burning characteristics of wildland fuels under field-relevant conditions so that the behavior of wildland fires can be better understood.

To satisfy the need for an intermediate-scale facility, the Wildland Fire Integrated Research Experiment (WildFIRE) facility, shown in Figure 3.1, was developed at the Auburn University Combustion Physics Lab (AUCPLab). The WildFIRE facility is capable of burn areas up to 0.8 m^2 and bridges the gap between traditional bench-scale experiments, which typically characterize the fundamental properties of the fuel, and full-scale research fires conducted by government labs, which are on the scale of kilometers. The WildFIRE facility is optically accessible to allow for tracking the fire propagation rate, flame geometry, and flame burning intensity. The facility integrates these optical diagnostics with simultaneous measurements of fuel mass consumption rate, temperature, and pollutant emissions.

This study specifically focused on the effects of initial fuel loading on the burning characteristics of loblolly pine straw (*Pinus taeda* L.). Loblolly pine straw was selected as the fuel for this study because its range covers more than 6.3 million ha of the Southeastern United States and more hectares are planted of it each year in the US than any other species [5, 6]. The Southeastern United States also has one of the lowest mean fire intervals with fires occurring every two to six years on average [7]. It is therefore crucial to understand how wildfires behave with fuels common in the Southeastern United States such as loblolly pine straw.

Chapter 2

Previous Work

Much work has been done over the last 80+ years to study and understand the behavior of wildland fires under a multitude of burning conditions and scenarios. This section will present an overview of some of the hallmark research conducted in the field of experimental wildland fire research during this time. Studies have been conducted across a range of sizes including bench scale chemical kinetics experiments on the scale of centimeters, laboratory-scale wildland fire burns on the scale of one to ten meters, and full-scale field burns on the scale of tens of meters. A variety of diagnostics techniques have been employed including load cells, thermocouples, and heat flux sensors. In more modern studies, optical diagnostics have seen much use including the use of visual cameras, thermographic cameras, stereovision systems, and particle image velocitmetry. These techniques have been used to measured important wildland fire characteristics such as fuel mass consumption rate, fire spread rate, heat flux ahead of the fire, flame temperature, and the geometrical shape of flames. This section will present an overview of these studies.

2.1 Chemical Kinetics Studies

Small scale laboratory studies have been conducted to study the chemical kinetics properties of wildland fuels. Such studies use thermogravimetric analysis (TGA) and calorimetry to measure important chemical kinetic properties that are necessary inputs to wildland fire spread models. In the case of TGA, the activation energy and pre-exponential factors are determined for use in the Arrhenius reaction rate equation. Elder et al. used thermogravimetric analysis to study grass species

common in the longleaf pine ecosystem [8]. Leyroy et al. applied TGA to measure the chemical kinetics of a number of Mediterranean scrub species [9]. Rovira et al. studied forest litter from European pine forests at six stages of decomposition and found that activation energies decreased with degradation [10]. Amini et al. determined the pyrolysis kinetics for fourteen different plant species using TGA, both live and dead, which are all native to forests in the United States [11].

Calorimetry has also been used to study the chemical properties of wildland fuels. Calorimetry allows for the measurement of the heat of combustion and heat of reaction. In the case of heat of combustion, a wildland fuel sample is burned in an oxygen atmosphere and the amount of energy released from the combustion is measured. Fro the heat of reaction, the process is similar except the test is done it a nitrogen atmosphere and the focus is on measuring the amount of energy required to fully pyrolyze the fuel sample. The heat of reaction and heat of combustion are strongly linked to how well a particular fuel will sustain combustion. Dickinson et al. used calorimetry to measure the heat of combustion of oak and maple samples taken from different locations. The focus of their study was to determine how the topographical location of the fuel sample was taken from affected the heat of combustion for the purpose of making inferences about how topographical location of fuel could potentially affect the spreading behavior of a fire [12]. White et al. reported results from cone calorimetry tests on landscaping plants in California, a number of tree and understory species from Colorado, and native and invasive plants from the northeastern United States [13]. The heats of reaction and combustion combined with activation energies and temperatures provide essential information regarding the chemical kinetics of the wildland fuel combustion such that accurate physical and empirical models can be developed to simulate the burning of wildland fires.

2.2 Macroscopic Fire Property Studies

While the chemical kinetics properties provided by TGA and calorimetry are valuable, equally as necessary is the study of the more macroscopic properties of wildland fires such as flame geometry, flame temperature, fire spread rate, fireline intensity, mass loss rate, and fuel consumption

efficiency. Tests have been carried out under both laboratory and field scales to study the effects of environmental and fuel conditions such as fuel loading, fuel moisture content, slope, and wind on the burning characteristics of wildland fires.

Prior et al. investigated whether the flammability of grass and litter fuels contributed to the different patterns of landscape fire activity around the world [14]. Prior et al. state that grass is highly flammable and burns rapidly, whereas litter fires spread more slowly but are likely to burn for longer. For this study, dried fuel samples were placed in a circular tray with a diameter of 26 cm and 4.6 cm high walls. The tray was placed in a small, open-fronted shed with a fiber cement shelf to minimize air movement and a cotton ball soaked in denatured alcohol was placed in the center of the sample for ignition. Time to ignition was recorded as the time between ignition of the bottom ball and visible ignition of the fuel sample. Rate of spread was determined by measuring the amount of time it took the flames to reach the edge of the tray and dividing by tray radius. A video camera was used to record the flame and flame heights were determined from the video footage by observing the flame height relative to a ruler placed in the video frame. Two thermocouples, one placed at 5 cm and another at 30 cm above the fuel sample were used to measure temperature. The mass was measured before and after the burn and mass consumption rate was calculated as the mass consumption divided by the flaming duration. Results showed that the rate of combustion and mean flame height were positively correlated with each other, and negatively correlated with flaming duration.

Fonda studied the burning in needles from eight pine species [15]. Four of the species studied are fire resisters able to survive the direct effects of wildfires: Ponderosa pine (*Pinus ponderosa*), Jeffrey pine (*Pinus jeffreyi*), Longleaf pine (*Pinus palustris*), and south Florida slash pine (*Pinus elloittii var. densa*). The other species studied are fire evaders, which are killed by wildfire, but survive on the post-fire site via seed germination: Monterey pine (*Pinus radiata*), knobcone pine (*Pinus attenuata*), sand pine (*Pinus clausa*), and jack pine (*Pinus banksiana*). Fonda measured flame height, flame time, ember time, burn time, percent fuel combustion, and mean rate of weight loss. Samples of needles weighing 18 g were burned in a 1 m x 1 m x 3 m tall facility. A four

story tall chimney was used as the exhaust and induced a mean air velocity over the needles of 9.9 cm/s. The pine needles were arranged on a 35 x 35 cm grid of xylene soaked strings. Flame height was observed by two people against a 2 m rule on the rear wall of the fire chamber. Timers were used to measure the time it took from ignition until all flames were extinguished, and the time from ignition until all embers were extinguished. The difference between the two was then taken to be the ember time. Results showed that longleaf pine, ponderosa pine, and south Florida slash pine had the highest values for flame height, percent fuel combusted, and mean rate of weight loss. Knobcone pine and Monterey pine had the longest ember time and burn time. Sand pine and jack pine had the longest flame time. Fire resisters tested highest in flame height, percent fuel combusted, and mean rate of weight loss. Evaders had greater flame and burn times. Westerner pines were found to be significantly greater than eastern pines in all burning characteristics except flame time and mean rate of weight loss.

One of the most important fire characteristics is the fireline intensity, which represents the rate of heat release per unit time per unit length of the fire front, regardless of its depth [16]. Fireline intensity is widely used as a measure in forest fire applications to evaluate the effects of fuel treatment on fire behavior, to establish limits on prescribed burning, and to assess fire impacts on ecosystems [16]. Due to the importance of fireline intensity as a measure of wildland fire, multiple studies have developed methods to measure the heat release from fires experimentally.

Morandini et al. conducted a series of experimental fires in a laboratory environment in a closed room without airflow across pine needles beds on a dedicated combustion table [17]. The combustion table was 1.5 m long and 1 m wide, made of wood, and insulated on top with refractory cement. Fuel beds of *Pinus pinaster* with a fuel loading of 0.5 $\mathrm{kg/m^2}$ were placed in the middle 0.5 m of the tray. Sixteen thermocouples located along the vertical direction in the center of the fuel bed and six more thermocouples located inside the fuel bed along its horizontal direction were used to measure temperature. An IR camera operating in the 3 to 5 $\mu\mathrm{m}$ band was used to record the experimental runs. Two heat flux sensors were located at the end of the bed of pine needles. The mass loss of the fuel particles were measured using a quick response high-precision

balance. Results saw two temperature peaks, the first one being the gaseous combustion zone delimited by the pyrolysis front and a char combustion zone. Between the two high temperature zones Morandini et al. report a cooler zone where an oxygen depleted environment prohibits char oxidation.

Santoni et al. presents a series of experiments conducted in a facility dubbed the Large Scale Heat Release Calorimeter (LSHR) to provide the fireline intensity for unsteady spreading fires [18]. The LSHR provides the unique ability to measure the heat release of free burning laboratory-scale wildland fires. Heat release is estimated by using a gas analyzer located in the exhaust duct to measure the amount of oxygen depletion in the exhaust stream. To do this, the combustion of pine needles was represented by the stoichiometric reaction for the complete combustion of lignocellulosic materials. Results demonstrate that the heat of combustion determined using oxygen-bomb calorimetry rather than oxygen depletion calorimetry during free burning vary considerably. Since the experiments were conducted under well-ventilated conditions, the results were used to generate a formulation for the heat release rate based on mass loss rate.

Morandini et al. further extended this work to investigate the radiant and convective heat release from the fires [19]. Results showed that radiation was the dominant mechanism in the preheating zone with some transfers combining radiation and convection were noted closer to the flame front. Morandini et al. found that fuel loading had a significant impact on the thermal degradation of the fuel litter and on the resulting fire properties. Heat release rate, the burning rate, and the rate of spread were all found to increase with fuel loading. The radiant fraction was found to be around 9.7% and decreased with increasing fuel loads. The convective fraction was also found to decrease as fuel loading was increased.

2.2.1 Slope Effects

Tihay et al. used the LSHR to conduct a study on the influence of fuel load and slope on a fire spreading across a 1 m x 2 m bed of *Pinus pinaster* needles using oxygen consumption calorimetry [20]. The study of slope effects on wildland fire is important since slope is among the most

influential factors affecting the spread of wildfires [21]. Tiyah et al. placed the beds on a 2 m long by 2 m wide combustion table located under a 3 m x 3 m fume hood with a 1 m^3/s extraction rate [20]. Fuel loadings of 0.6, 0.9, and 1.2 kg/m^2 were tested and experiments were conducted with either no slope or 20°slope. The flame spread rate, flame length, flame height, and flame angle were determined from photographs taken every 2 to 4 seconds. Heat release rate was measured using the oxygen depletion technique and the mass loss rate was measured using a load cell upon which the bench was located. Results showed that the flame length and rate of spread increase when fuel load or slope increases. The heat release did not reach a quasi-steady state when the propagation takes place with a slope of 20°and a high fuel load due to an increase in the length of the fire front leading to an increase in fuel consumed. Results further showed that flame height increased with fuel loading as did the flame spread rate. The spread rate was found to asymptotically approach a maximum value, which was linked to the scale of the combustion table. Mass loss rate was found to be linear for the no-slope cases and increase over time for the 20°cases.

Dupuy conducted a set of laboratory experiments in *Pinus pinaster* and *Pinus halepensis* litters to investigate the effects of slope on fire behavior for different levels of fuel loading [22]. The range of slopes studied ranged from -30°to 30°. The rate of spread and mass loss rates were observed when the fire was in a quasi-steady state. The experiments were conducted on an experimental apparatus consisting of an aluminum plate insulated with sand or asbestos sheets. The plate was palced on an electronic scale and could be adjusted to a range of angles. Fuel loadings ranged from 0.4 to 1.2 kg/m^2 with a step size of 0.2 kg/m^2 for *Pinus pinaster* and from 0.4 to 1.2 kg/m^2 with a step size of 0.4 kg/m^2 for *Pinus halepensis*. Results show that the rate of spread is well fitted using a power law of the form $R\ w_o^b$, where w_o is the fuel loading, and the mass loss rate was then fit by $R\ w_o^{b+1}$. Results show that Rothermel's model for wildland fire spread [23] predicts the rate of spread as a linear function of fuel load, but that experimental results did not show this behavior. Dupuy concludes this to be due to the Rothermel model assuming constant resident time with fuel load, where resident time represents the time it takes the fire to burn from the bottom of

the fuel bed. Dupuy suggests instead resident time should be viewed as a power function of fuel depth.

Dupuy et al. presented a study on the effects of fuel bed width and slope using laboratory-scale fires [24]. *Pinus helepensis* fuel beds with 1 $\mathrm{kg/m^2}$ fuel loading were used. Experiments were conducted on a 10 m long and 4 m wide inclinable table with an area available for burning of 3 m wide and 9 m long. A top-rear camera view was used to determine the fireline contours, airflow patterns, and flames. Solid material remaining after complete fire extinction was collected to measure the fuel consumption. Air and flame temperature were measured using nine vertical arrays of six thermocouples. Rate of spread was found to be steady for 0°to 10°fires and unsteady in 20°to 30°upslope fires.

Silvani et al. carried out a series of experiments on a large-scale bench with an inclinable plate to study the effect of slope on fire spread [25]. These experiments were conducted at the same facility as in [24]. The fuel bed was made from 7 m long and 3 m wide beds of excelsior with fuel loading maintained constant at 0.4 $\mathrm{kg/m^2}$. Slope angles of 0°, 20°, and 30°were tested. Two cameras were used to record each experiment from a side and top view. The lateral view of the fire provided data on the height and tilt of the flame front while the topside view provided data on the rate of spread and the shape of the fire front. Gas temperatures were measured using thermocouples. Results showed that as slope increased the radiation dominated thermal environment turned into a mixed convective-radiative one, where convection finally dominated for steep slope configurations. This is in agreement with the critical slope angle of 24°as presented by Wu et al. [26]. Silvani et al. note that convective heat transfer was present all along the flame front, even for flat terrain [25].

Morandini et al. conducted a study on laboratory-scale fires spreading across a 0.85 m long and 0.45 m wide fuel bed of excelsior [21]. This study was unique for its use of advanced optical diagnostic techniques including PIV and OH* chemiluminescence. The PIV technique used was originally introduced by Morandini et al. [27] and was used to investigate the 2D velocity field of the reacting flow. A similar PIV technique was previously used by Lozano et al. to study the fluid

dynamics structures within the flame spreading across a bed of aspen (*Populous tremuloides Michx*) excelsior [28]. However in this study by Lozano et al. the flame contour could not be located within the velocity field, which made it hard to localize the area ahead of the flame front [21]. In the study by Morandini et al. OH* chemiluminescence is used to locate the contour of the reacting zone within the computed velocity field [21]. OH* chemiluminescence imaging in the UV range allowed the filtering of any incandescent radiation from soot or solid fuel and any thermal radiation from hot parts to provide instantaneous images of the gaseous reaction zone. Results showed that the increase in the rate of fire spread with increasing slope is attributed to a significant change in fluid dynamics surrounding the flame. Later, Morandini et al. conducted more tests using this PIV technique on a larger bed of excelsior 7 m long and 3 m at fuel loads of 0.2, 0.4, and 0.6 $\mathrm{kg/m^2}$ [29].

Motivated by the need for an increased understanding about the relative roles of radiant and convective heating in fire spread, Tihay et al. [30] used the Large Scale Heat Release (LSHR) calorimeter facility to measure the heat release, mass loss rate, flame geometry, and heat transfer for forest litters under slope conditions. This work was an extension of the previous work done with the LSHR facility [19, 31]. Results show that the mass loss rate does not reach a steady state when the propagation takes place under slope conditions.

Zhou et al. studied the effect of terrain slope on marginal burning in live chaparral shrub fuel beds [32]. Results showed that upslope fire spread depends not only on the increased radiant heat transfer but also on the aerodynamic effects created by the interaction of the flames with the slope.

The burning of live fuels has been studied as well, which burn differently than the dead fuel beds used by most studies. Weise et al. assessed how well common fire spread models predicted a fire burning through life fuels [33]. The effects of wind velocity, fuel moisture content, and fuel bed depth were studied on the flame propagation in 2 m long by 1 m long fuel beds containing one of four species of live chaparral shrub species. Results found that most wildland fire prediction models did a sub-standard job of predicting the spread of wildland fire through live fuels.

2.2.2 Wind Effects

The effect of wind on the burning of wildland fires has been studied as well. Wind is one of the most important factors driving spread rate. Multiple facilities have been developed over the last 80 years to study wind driven fires in the laboratory, typically using a wind-tunnel style burning facility. Some field studies have also been conducted.

Catchpole et al. conducted a series of 357 experimental fires to study the rate of spread in free-burning fires in woody fuels in a wind tunnel located at the US Forest Service's Intermountain Fire Sciences Laboratory [34]. The facility had a 3 m cross-section providing control of wind speed, temperature, and relalative humidity. Fuel was burned in a burning tray that was 5 to 8 m long. The fires were burned over a large range of particle sizes, fuel bed depths, packing ratios, moisture contents, and wind speeds. The time interval and passage of the flame was recorded using photo-cells and an image analysis system was used to determine flame height, length, depth, and tilt angle. The results showed that fire spread rate decreases with moisture content in a way that depends on the fuel type and diameter. Spread rate was found to decrease as the square root of the packing ratio. Fuel bed depth was found to have little effect on the spread rate. Fuel diameter was found to only have a significant effect for fuels above 1 mm. The relationship between wind and spreadrate was found to be virtually linear.

Mendes-Lopes et al. carried out an extensive set of experiments in a low speed wind tunnel to study fires propagating in 2 m x 0.7 m beds of *Pinus pinaster* needles [35]. Wind velocity, fuel moisture content, and slope were varied. Optical diagnostics were used to measure flame height, flame length, flame angle, and rate of spread. Temperature measurements were taken using a tower of thermocouples at multiple heights above the fuel bed. Results showed that the rate of spread of fires burning in the direction of the wind increased rapidly with wind speed for wind-driven fires, that spread rate did not depend on wind speed for fires burning against the direction of the wind. Rate of spread was found to decrease with increasing fuel moisture content. Flame angle and flame height were found to be dependent on velocity, slope, and fuel moisture content.

Anderson et al. used the same 3 m x 3 m x 26 m wind tunnel as Catchpole et al. [34] located at the USDA Forest Service Fire Sciences Laboratory in Missoula, Montana, USA to investigate the convective heat transfer ahead of a steadily progressing fire front [36]. Fuel beds were placed on a 1 m wide 7.5 m long fuel tray centered in the floor of the tunnel. Rate of spread of the fire was measured via photo-cells, temperature measurements were taken using multiple thermocouples, and wind velocity was measured using kiel-static probes. The effects of fuel and environmental variables on the gas temperature profile and the surface wind speed were investigated. In non-zero winds, the temperature of the air near the fuel beds was found to decay exponentially with distance from the fire front. In zero winds, the temperature was found to decrease rapidly within a very short distance of the flame front, then decay slower as distance from the flame front continued to increase. The maximum air temperature was found to decrease as the free-stream wind speed, packing ratio, and fuel moisture content increased.

Field-scale experiments on the effect of wind on wildland fire burning have been conducted as well. Morandini et al. conducted a series of experiments to study the influence of wind on flame front properties in fire spread across Mediterranean shrub [37]. The main motivation for this study was to generate field-scale data that could be used to validate models since laboratory-scale fires are not sufficient to study some fire effects, such as turbulence, that only occur on large-scale fires. The study demonstrated that it is possible to measure thermodynamic properties of a fire in the field. The fuel plots for this study were 30 m wide and 80 m long consisting of 2.5 m high Mediterranean shrub vegetation. Flame temperature and radiation emitted ahead of the flame front were measured. Three 2D ultra-sonic anemometers were placed around the plot to measure the wind fluctuations. Fire spread was recorded using three digital video cameras and an infrared camera. Results show that large scale turbulence influence the fire spread and affects the flame shape, temperature, and radiation emission.

2.2.3 Fuel Moisture Content

Fuel moisture content has been studied as well. Davies et al. conducted a series of small, field-based ignition tests on 2 m x 2 m plots to study the flammability of *Calluna vulgaris* [38]. The study found that at moisture contents above 70%, both spot and line ignitions failed, but where moisture content was less than 60%, fires developed rapidly.

Awad et al. conducted a series of fire spread experiments in 1 m wide and 2 m long beds of excelsior (shredded *Pinus*) [39]. Fuel loadings of 0.15, 0.2, and 0.4 $\mathrm{kg/m^2}$ were studied to determine the moisture content threshold that leads to extinction. Results showed that fire extinction is primarily affected by fuel moisture content and fuel loading, and that fuel moisture content threshold increases with fuel loading and this threshold tends to become independent of the load with high fuel loadings.

Many studies have used similar burning table type experiments to the one used in the present study. Thermocouples, load cells, and optical diagnostics have frequently been used to measure the wildland fire burning characteristics of a variety of fuels. Multiple fuel types have been studied as well. Some species of pine needles have been studied, but a large focus has been on species native to the Mediterranean region and the chaparral shrub in California. Not many studies have focused on wildland fuels common to the south east United States, particularly longleaf pine (*Pinus palustris*) and lobolly pine (*Pinus taeda*). As such, the present work will employ a similar burning table style experimental facility as has been successfully used in previous works to study the wildland fire burning characteristics of loblolly pine straw. This work contributes to the existing literature by fulfilling the need for meaningful intermediate-scale data via an analysis of wildland fire by simultaneously measuring the burning characteristics using both traditional and optical diagnostic techniques. These results will help researchers better understand the behavior of wildland fires and provide data that can be used to develop informed policies regarding risk management of wildland fires using techniques such as prescribed burning. Additionally, the results presented in this study are useful as validation data to assess the accuracy and performance wildland fire modeling codes.

Chapter 3

Experimental Methods

3.1 The Wildland Fire Integrated Research Experiment

The Wildland Fire Integrated Research Experiment (WildFIRE) developed as part of this study is shown in Figure 3.1. The test section is 1.8 m long, 0.6 m wide, and 0.9 m high. The facility is open on the top and ends, and closed on each length-wise side. The floor of the facility is a 6.35 mm thick aluminum plate hung from two load cells which provide mass consumption data during burning experiments. One length-wise sidewall of the facility is made from 6.35 mm thick tempered glass, allowing access for optical diagnostics. The other length-wise sidewall is 6.35 mm thick aluminum painted black to provide a solid, non-reflective background with high contrast for optical diagnostic techniques. The height of the facility was designed such that the maximum flame height would not extend out of the top of the facility for the test conditions investigated as part of this study.

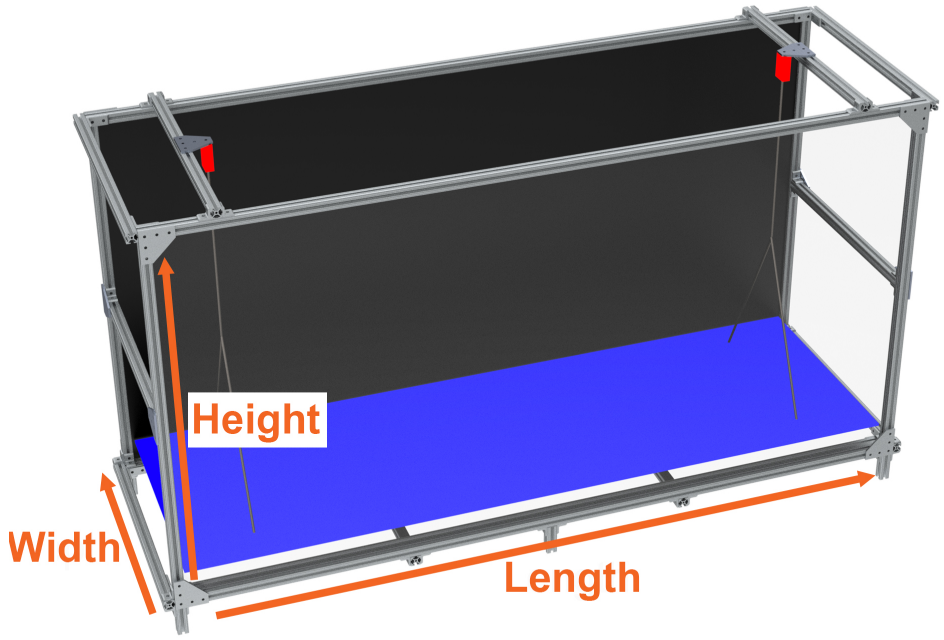

Figure 3.1: Computer Graphics Rendering of the WildFIRE Facility. The load cells and weight plate are highlighted in red and blue, respectively.

The goal of these experiments was to determine the effect of initial fuel loading on the burning characteristics of loblolly pine straw. Fuel loading was calculated as the initial fuel mass divided by the surface area of the floor. Table 3.1 shows the fuel loadings investigated in this study along with the associated initial fuel mass and fuel bed thickness. The actual fuel loading for each test varied slightly from the target fuel loading due to experimental error, but in all cases the actual fuel loading was within 5% of the target value. The variations from the target value are also shown in Table 3.1. The specific burning characteristics measured were the fuel mass consumption rate, flame temperature, CH* flame intensity, fire propagation rate, flame height, flame length, flame surface area, and the pollutant emissions released by the fire.

Loblolly pine straw with a nominal moisture content of 10% by mass calculated on a dry basis was used as the fuel for all tests. The length and width of the fuel bed was maintained as a constant 124.46 cm and 55.88 cm, respectively, resulting in a burn area of 0.695 m^2 for all of the tests. The thickness of the fuel bed, shown in Table 3.1, was allowed to change such that the bulk density was

kept to a nominal value of 20.5524 $\mathrm{kg/m^3}$. While efforts were made to maintain the bulk density as close to the nominal value as possible, in reality the bulk density for each test changed due to slight differences in the actual versus target initial mass value for each test. The mean actual bulk density was 20.3912 $\mathrm{kg/m^3}$ with a standard deviation of 0.3722 $\mathrm{kg/m^3}$ and a maximum variation of 4.7% from the mean value. The bulk density was calculated by dividing the fuel mass by the volume of the fuel bed. The bulk density was controlled by placing a plywood board having the same length and width as the fuel bed on top of the fuel bed using spacers. The bulk density of the fuel bed was then set by compressing the board against spacers having the desired fuel bed thickness for each test. The packing ratio was calculated as the bulk density divided by the density of loblolly pine straw to be 0.0402. The density value used for loblolly pine straw was 511 $\mathrm{kg/m^3}$.

For each test, the fuel bed was ignited using a piece of cotton string soaked in denatured alcohol and placed along the width of one end of the fuel bed to ensure even and simultaneous ignition. All tests were conducted indoors under a canopy style fume hood so that all combustion products could be safely evacuated while also removing the environmental effects of testing outdoors. The fume hood was located 1 m above the top of the WildFIRE facility and had an opening of 1.8 m by 1.2 m. An Extech 407119 hotwire anemometer was used to measure the wind velocity induced by the fume hood. The wind velocity at the top of the WildFIRE facility was measured to be 0 ± 0.00508 $\mathrm{m/s}$. The extraction rate of the fume hood was measured to be 7452 $\mathrm{L/s}$.

Table 3.1: Fuel bed thickness for each initial fuel loading value tested. The experimental variation in actual fuel loading values compared to the target value is also listed.

Fuel Loading ($\mathrm{kg/m^2}$)	Initial Fuel Mass (kg)	Fuel Bed Thickness (cm)
0.98 ± 0.025	0.68 ± 0.017	4.76
1.31 ± 0.063	0.91 ± 0.044	6.35
1.63 ± 0.034	1.13 ± 0.024	7.94

3.2 Data Acquisition

The WildFIRE facility was designed to enable simultaneous synchronized measurements of multiple wildland fire burning characteristics. The facility was outfit with load cells to measure fuel mass, an array of fine-wire thermocouples to measure the temperature of the fire, a gas analyzer to measure the concentrations of multiple pollutants produced by the fire, and a scientific camera to measure the geometry and chemiluminescent intensity of the flame. In order to acquire data from all of these sources simultaneously, a data acquisition system was assembled using National Instruments (NI) data acquisition hardware. In particular, a NI cDAQ-9137 was equipped with a NI 9237 load cell module and NI 9213 thermocouple module to acquire the fuel mass consumption and flame temperature data. The gas analyzer was connected to the cDAQ-9137 via a serial connection. The scientific camera was connected to a separate desktop computer used to record the video. A custom LabVIEW data acquisition program was written leveraging NI DAQmx to acquire data from the load cells and thermocouples, NI VISA to interface with the gas analyzer via a serial protocol, and the Ximea LabVIEW API to acquire data from the scientific camera.

The user interface of the developed data acquisition program is shown in Figure 3.2. The load cell data (outlined in red), thermocouple data (outlined in blue), and emissions data (outlined in green) are all displayed to the user. The program allows the end user to see a quick overview of all of the measured burning characteristics during testing. Additionally, the program allowed the user to start acquiring data simultaneously from all sources by pressing a single button, greatly simplifying the data acquisition process. Data files are automatically named based on the current date and time, further automating the data acquisition process.

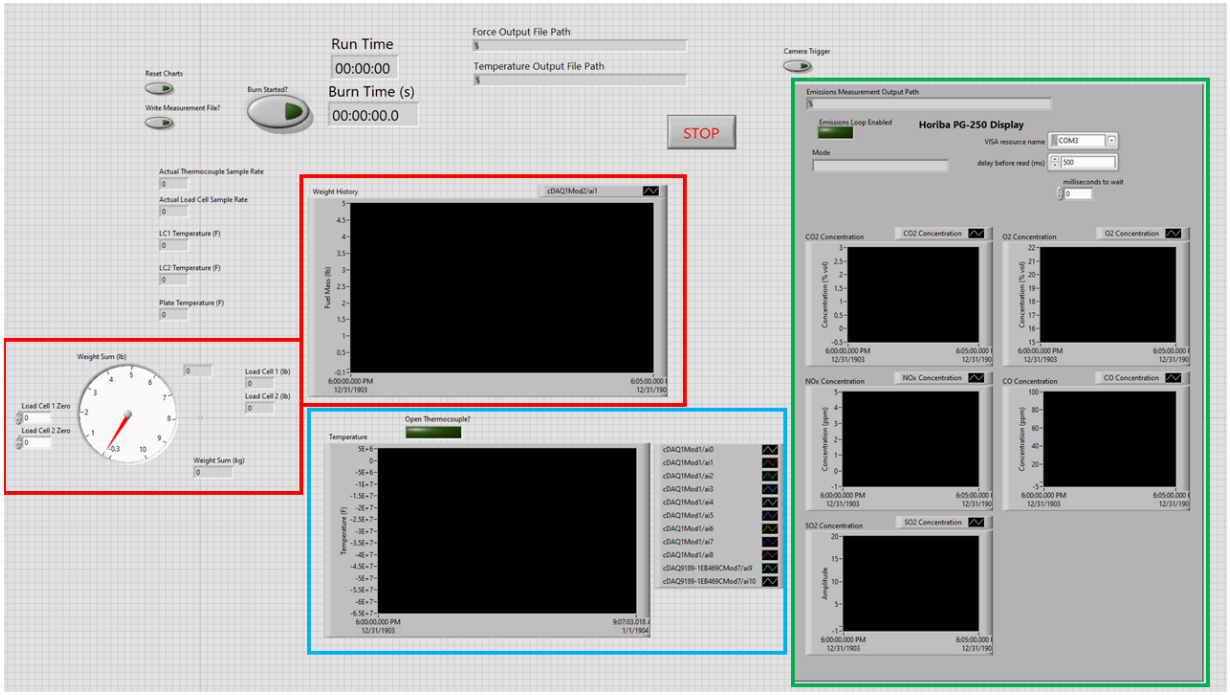

Figure 3.2: The LabVIEW control panel for the WildFIRE data acquisition program.

3.3 Data Processing

To account for variations in the conditions between tests and to gain insight into the repeatability of the tests, ten burns ($n_s = 10$) were conducted for each fuel loading group. The sampled values of each burning characteristic at each point in time were averaged across all burns for a given fuel loading using

$$\mu_{X,\mathrm{FL}}(t) = \frac{\sum_{i=1}^{n_s} X_i(t)}{n_s}, \tag{3.1}$$

where $\mu_{X,\mathrm{FL}}(t)$ is the mean of burning characteristic X as a function of time for the $n_s = 10$ tests at each fuel loading (FL), and $X_i(t)$ is the recorded burning characteristic as a function of time for a given test i. The burning characteristic (X) can be one of the following: fuel mass (m), flame intensity (I), flame front location (L), flame height (H), flame length (W), flame surface area (A), or pollutant concentration (χ). The standard error of the mean was then calculated using

$$\mathrm{SE}_{X,\mathrm{FL}}(t) = \frac{\sigma_{X,\mathrm{FL}}(t)}{\sqrt{n_s}}, \tag{3.2}$$

where $\mathrm{SE}_{X,\mathrm{FL}}(t)$ is the standard error of the mean, $\sigma_{X,\mathrm{FL}}(t)$ is the standard deviation, and n_s is the number of tests run at each fuel loading. The standard deviation was calculated as

$$\sigma_{X,\mathrm{FL}}(t) = \sqrt{\frac{\sum_{i=1}^{n_s} \left(X_i(t) - \mu_{X,\mathrm{FL}}(t)\right)^2}{n_s}}. \tag{3.3}$$

Confidence intervals were calculated for each measured characteristics with a confidence of 95% as

$$\mathrm{CI}_X(t) = \mu_{X,\mathrm{FL}}(t) \pm (t_s)\,\mathrm{SE}_{X,\mathrm{FL}}(t), \tag{3.4}$$

where CI_X is the 95% confidence interval of burning characteristic X and t_s is the t-value.

Next, the mean of each burning characteristic was calculated for for each fuel loading by taking the mean of the individual burning characteristic for each test within a fuel loading group as

$$\overline{X}_{\mathrm{FL}} = \frac{\sum_{i=1}^{n_s} X_i}{n_s}, \tag{3.5}$$

where $\overline{X}_{\mathrm{FL}}$ is the mean burning characteristic for a given fuel loading, X_i is the burning characteristic for a specific test i, and n_s is the number of tests at each fuel loading. The burning characteristic (X) can be mean burn rate ($\overline{\dot{m}}$), residual mass fraction (η), the maximum temperature measured by the j row of thermocouples (T_j), the mean intensity ($\overline{I}$), the mean propagation rate ($\overline{\dot{L}}$), the mean flame height ($\overline{H}$), the mean flame length ($\overline{W}$), the mean flame surface area ($\overline{A}$), or the mean pollutant concentration ($\overline{\chi}$). The standard error of the mean burning characteristic for each fuel loading was calculated as

$$\mathrm{SE}_{\overline{X},\mathrm{FL}} = \frac{\sigma_{\overline{X},\mathrm{FL}}}{\sqrt{n_s}}, \tag{3.6}$$

where $\mathrm{SE}_{\overline{X},\mathrm{FL}}$ is the standard error of the mean burning characteristic for a given fuel loading and $\sigma_{\overline{X},\mathrm{FL}}$ is the standard deviation of the mean burning characteristic across n_s tests at that fuel

loading. The standard deviation was calculated as

$$\sigma_{\overline{X},\mathrm{FL}} = \sqrt{\frac{\sum_{i=1}^{n_s}\left(X_i - \overline{X}_{\mathrm{FL}}\right)^2}{n_s}}. \tag{3.7}$$

Lastly, the 95% confidence interval was calculated as

$$\mathrm{CI}_{\overline{X}} = \overline{X}_{\mathrm{FL}} \pm (t_s)\,\mathrm{SE}_{\overline{X},\mathrm{FL}}, \tag{3.8}$$

where $\mathrm{CI}_{\overline{X}}$ is the 95% confidence interval for the mean burning characteristic for a given fuel loading.

The subsequent sections will describe how each of the aforementioned burning characteristics (X) were obtained prior to being processed using the described methodology.

3.4 Mass Consumption Measurements

Fuel mass consumption rate was monitored via two Omega LCCA-50 load cells from which the floor of the WildFIRE facility was suspended. The load cells used have a 50 lb (22.68 kg) maximum capacity with an accuracy of 0.037% full-scale output, resulting in an effective accuracy of $\pm 8.391g$. Surface mount thermocouples mounted to the load cells were used to ensure that the load cells did not exceed their rated operating temperature of 150 ^{o}F (65 $^\circ$C) during testing. Actual load cell temperatures during testing ranged from 21 $^\circ$C to 49 $^\circ$C. The load cells were mounted to the top of the facility and the floor was hung using wire rope from the load cells as shown in Figure 3.1. This hanging-style configuration was chosen to prevent thermal expansion of the aluminum plate used as the floor from adversely affecting fuel mass measurements. The load cells were tared prior to fuel addition, which resulted in a measurement of the mass of any fuel added to the floor. The force reported from each load cell was monitored at a rate of 1612.9 Hz over the duration of the test. The raw load cell data was resampled onto a uniform 2 Hz time base to remove noise and serial correlation in the data before being further processed. The readings from each load

cell were then added together to provide the total fuel mass. The sampled mass values at each point in time were averaged across all burns for a given fuel loading using Equation 3.1 where, in this case, $X = m$. The 95% confidence interval of the mean burn rate as a function of time was then calculated using Equation 3.4. For each test, the mean burn rate, $\overline{\dot{m}}_i$, was calculated as the slope of a linear curve fit using the least squares method through the steady-state region of mass loss curve of that test. Next, the mean burn rate for each fuel loading was calculated by taking the mean of the individual mean burn rates for each test within a fuel loading group using Equation 3.5 with $X = \overline{\dot{m}}$. The 95% confidence interval of the mean burn rate for each fuel loading was calculated using Equation 3.8.

Lastly, the residual mass fraction was determined using the remaining mass after each test as

$$\eta_i = \frac{m_{f,i}}{m_{o,i}}, \tag{3.9}$$

where η_i is the residual mass fraction, $m_{f,i}$ is the final fuel mass, and $m_{o,i}$ is the initial fuel mass for a given test i. The mean residual mass fraction for each fuel loading was then calculated using Equation 3.5 with $X = \eta$. The 95% confidence interval of the mean residual mass fraction was calculated using Equation 3.8.

3.5 Temperature Measurements

Temperatures were measured at multiple locations using an array of nine fine-wire thermocouple probes sampled at a rate of 75 Hz. Before further processing, the thermocouple data was resampled onto a uniform 5 Hz time base. The thermocouples used were Omega model number KMQSS-062E-12, 0.0625 inch (1.6 mm) diameter, exposed junction, 12 inch (30.5 cm) long K-type thermocouple probes with an accuracy of ± 2.2 °C or 0.75% over a range of 0 to 1250 °C. The thermocouple probes were arranged in a grid formation and inserted through the side wall of the WildFIRE facility so that the tip of each thermocouple was in the mid-plane of the width of the fuel bed. Inserting the thermocouples through the side wall in this fashion ensured that the

weight of the thermocouple probes was supported cantilever style and did not adversely affect the fuel mass measurement. The grid of thermocouples was positioned within the facility as shown in Figure 3.3. The thermocouple spacing was chosen such that there would be a measurement of the temperature profile starting in the fuel bed and going up through the height of the flame. This vertical rake of thermocouples was repeated three times along the length of the facility to provide the temperature profile as the flame front propagates along the fuel bed.

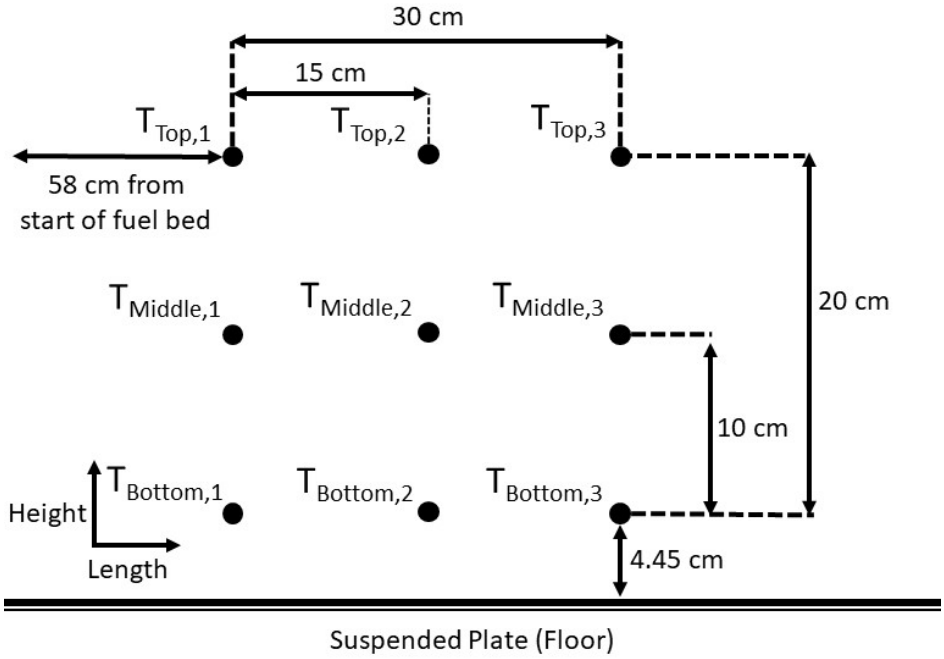

Figure 3.3: Diagram showing the locations of each thermocouple within the WildFIRE facility.

The thermocouple data was processed for each test to extract the maximum temperature measured across the three thermocouples in each row over the entire test duration as

$$T_{i,j,k} = \text{median}(\max 10(\tau_{i,j,k}(t))), \tag{3.10}$$

where $T_{i,j,k}$ is the maximum temperature measured by thermocouple k in row j during test i and $\tau_{i,j,k}(t)$ is the time history of that same thermocouple. In this case, the maximum temperature measured by each thermocouple during each test was calculated as the median of the highest 10

measured temperature values rather than simply taking the single highest temperature value to add robustness to the measurement. Next, the maximum temperature measured across all thermocouples in each row was calculated as

$$T_{i,j} = \max_{k=1}^{n_r}(T_{i,j,k}), \tag{3.11}$$

where $T_{i,j}$ is the maximum temperature measured by each row of thermocouples, j, during test i, and n_r is the number of thermocouples in each row. Once the maximum temperature for each row of thermocouples was determined for each test, the mean maximum temperature for each row of thermocouples for a given fuel loading was calculated using Equation 3.5 with $X = T_j$. The 95% confidence interval of the mean maximum temperature was then calculated using Equation 3.8.

3.6 Emissions Measurements

During burning, emissions data was acquired using a Horbia PG-250 gas analyzer to determine the effect fuel loading had on the potentially harmful emissions released from the fire. Specifically, concentrations of CO, NOx, and SO_2 were sampled. The PG-250 measures NOx using the chemiluminescence method, SO_2 using the non-dispersive infrared method, and O_2 using the galvanic cell method. The electrical response time of the gas analyzer was set to 10 seconds yielding a response time of less than 45 seconds for all cells except SO_2, which had a response time of within 4 minutes. Sample gas flow rate into the analyzer was 0.4 $\mathrm{L/min}$. Gas concentrations were recorded from the analyzer at a rate of 2 Hz. The analyzer inlet probe was positioned 35 cm above the floor of the facility and midway along the length of the burning surface for all tests. Emissions data was recorded throughout each test to measure the concentration of each pollutant at the probe location over time. Emissions data was processed by first adjusting the values to 15% oxygen as

$$\chi_{\mathrm{adj}} = \chi_{\mathrm{meas}}(20.9 - 15)/(20.9 - \%\mathrm{O_2}), \tag{3.12}$$

where χ_{adj} is the concentration adjusted to 15% oxygen, χ_{meas} is the original measured concentration, and $\%O_2$ is the % volume of oxygen measured by the gas analyzer associated with the original measured value. After adjusting to a 15% oxygen basis, the average concentration of each pollutant was calculated by integrating the measured concentration over time and dividing by the length of the test as

$$\overline{\chi} = \frac{\int_{t_o}^{t_f} \chi(t)\, dt}{t_f - t_o}, \tag{3.13}$$

where $\overline{\chi}$ is the average concentration of the pollutant being measured, $\chi(t)$ is the temporal history of the measured pollutant, t_0 is the start time of the test, and t_f is the end time of the test. Equation 3.5 was then used to average the average pollutant values for each test across tests within the same fuel loading group to arrive at an average value of each measured pollutant as a function of fuel loading.

3.7 Optical Diagnostics

High resolution video images of the fire were captured using a Ximea xiD MD061MU-SY CCD scientific camera. The camera was configured with a 50 mm focal length lens and positioned 5.7 m away from the glass side wall of the facility such that the entire length and height of the facility was captured within the field of view of the camera. Images were sampled at a rate of 10 Hz with a bit depth of 8 bits, and an exposure time of 100 ms. The lens was equipped with a 10 nm band-pass filter centered at 430 nm. This wavelength range corresponds to the CH* radical chemiluminescence wavelength and filtered out the light produced from soot and/or hot solid fuel species to effectively isolate the heat release. The brightness of each pixel in the images taken through the CH* filter is correlated with the line-of-sight integrated heat release of the flame at that location [40, 41].

In this study, the CH* chemiluminescence images were used to quantify intensity of the flame as a function of time, track the propagation of the fire along the length of the fuel bed, and measure the height, length, and surface area of the flame. An image processing code was developed to

extract these parameters from the raw flame images. The first step before any subsequent image processing was applied was to normalize the intensity of each pixel in the image by its maximum possible intensity. The maximum possible intensity of each pixel is determined by the bit depth of the image and was calculated as

$$I_{p,\max} = 2^{bd} - 1, \tag{3.14}$$

where $I_{p,\max}$ is the maximum possible intensity of each pixel, and bd is the bit depth of the image.

After the pixel intensities were normalized, the image processing code then determined the region within each image that represented flame. This was accomplished by converting the grayscale image to a binary image where each pixel was set to either true or false based on an intensity threshold. For this study, an intensity threshold was chosen such that pixels brighter than 15% of maximum brightness were marked as regions containing flame. This threshold value was chosen via trial and error such that the binary image corresponded with human observation of where flame areas were present. The threshold was kept as low as possible, to capture the maximum amount of flame while avoiding false positives. It is important to note that since the images were taken through a very narrow band-pass filter, nearly all extraneous light is eliminated and therefore any significant intensity value in the image can safely be assumed to represent the flame.

In the resulting binary image, pixels have a true value when they represent the flame and false value when they do not represent the flame. An example of this type of processing can be seen in Figure 3.4, which shows the raw flame image and its corresponding thresholded binary image. Once the binary image was generated, the CH* intensity, flame front location, flame height, flame length, and flame surface area were extracted.

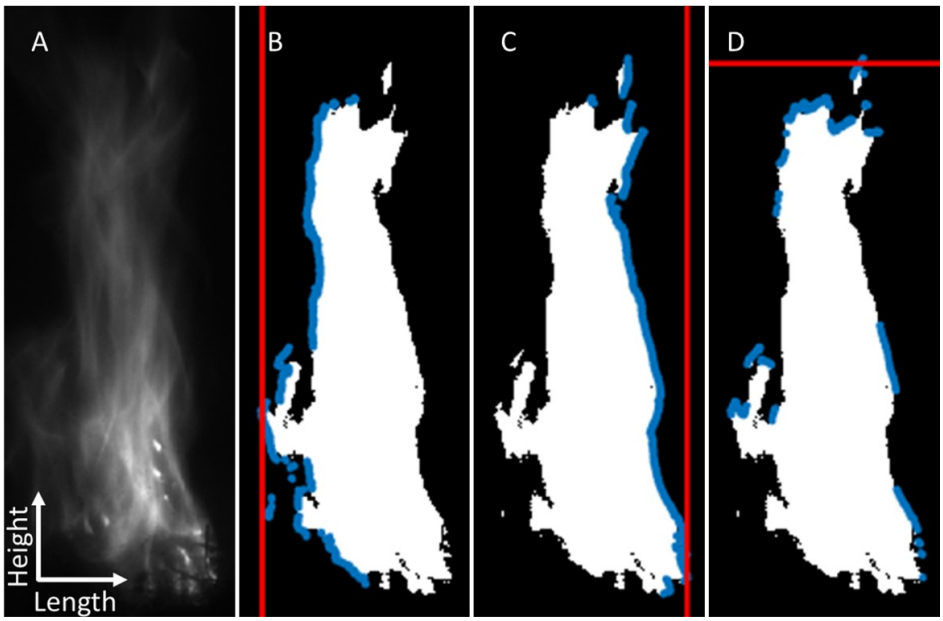

Figure 3.4: An example figure depicting how the flame detection processing works. Frame (a) shows the cropped monochrome flame image. Frames (b), (c), and (d) all show the resulting thresholded image along with the points identified on the rear, forward, and top edge of the flame, respectively. The red lines represent the location of the frame rear (b), flame front (c), and flame height (d).

3.7.1 Flame Intensity Measurements

The CH* intensity was calculated by summing the intensity of all pixels in the image identified as flame, i.e., the number of pixels with intensities greater than the threshold value. This intensity was then normalized by the number of flame pixels as

$$I_i(t) = \frac{\sum_{p=1}^{n_f} I_p(t)}{n_f}, \tag{3.15}$$

where $I_i(t)$ is the chemiluminescence intensity of the flame as a function of time for test i, n_f is the number of flame pixels in a given image, and $I_p(t)$ is the intensity of each flame pixel. The mean intensity as a function of time for each fuel loading was then calculated using Equation 3.1 with $X = I$. The 95% confidence interval of the mean as a function of time was then calculated using Equation 3.4.

Next, the mean intensity for the duration of each test, $\overline{I}_i$, was calculated as the mean of all intensity measurements taken during the steady-state region of that test. Finally, the mean intensity for each fuel loading was calculated by taking the mean of the individual mean intensities for each test within a given fuel loading group using Equation 3.5 with $X = \overline{I}$. The 95% confidence interval of the mean intensity for each fuel loading was calculated using Equation 3.8.

3.7.2 Flame Propagation Measurements

To determine the fire propagation rate, the forward-most edge of the flame front was identified in each image acquired to create a time history of the flame front as it propagated along the length of the fuel bed. To identify the flame front location, the image processing code searched each row of pixels in the binary image to find the forward-most "true" location corresponding to the forward most edge of the flame. Occasionally, reflections off metallic components of the WildFIRE facility or embers rising from the fire will have an intensity greater than the intensity threshold and thus get identified as flame. Figure 3.5 shows an example of one such outlier circled in red in the bottom left of the image.

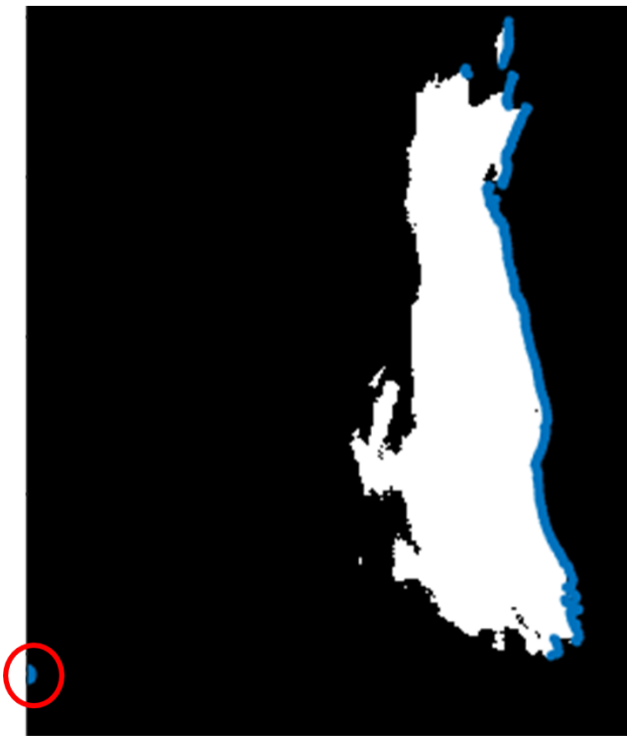

Figure 3.5: Shows an example of an outlier point (circled in red) being undesirably identified as flame.

In this case, the outlier was cause by reflections off one of the bolts fastening the suspension cables to the burning plate. Since these points do not lie on the edge of the flame contour, and the objective was to identify the edge of the flame, they are considered outliers. Rather than raise the intensity threshold for a pixel to be marked as flame, which would adversely affect the flame geometry measurements, the decision was made to implement an outlier removal algorithm. The outlier removal algorithm removed points with a distance of greater than three standard deviations away from the median value of all identified flame front points. Once outliers were removed, the median of the 10 forward-most points on the leading flame edge flame edge was taken to be the flame front location for each moment in time.

The mean flame front location as a function of time for each fuel loading was then calculated using Equation 3.1 with $X = L$. The 95% confidence interval was then calculated using Equation 3.4. For each test, the mean propagation rate, $\overline{\dot{L}_i}$, was calculated by applying a linear fit to the recorded flame front locations during the steady-state region of the test using a least squares

regression technique. Then, the mean propagation rate for each fuel loading was calculated by taking the mean of the individual propagation rates for each test within a given fuel loading group using Equation 3.5 with $X = \overline{\dot{L}}$. The 95% confidence interval of the mean propagation rate at each fuel loading was calculated using Equation 3.4.

3.7.3 Flame Length Measurements

The flame rear location was identified in an identical manner as to with the flame front location, except in this case the rearward-most "true" location in each row of pixels in the thresholded binary image was used. The outlier removal algorithm was applied, this time based on the distance from identified points to the median of all points identified on the rear edge of the flame. After outliers were removed, the median of the 10 rearward-most points on the rear edge of the flame were taken to be the flame rear location. Once the flame rear location was calculated, the flame length was taken to be the distance between the forward edge of the flame and the rearward edge of the flame.

The mean flame length and 95% confidence interval as a function of time for each fuel loading was then calculated using Equation 3.1 and Equation 3.4, respectively, with $X = W$.

3.7.4 Flame Height Measurements

Flame height was calculated by locating the points on the top edge of the flame and determining the height of these points relative to the bottom of the flame. Measuring the flame height relative to the bottom of the flame rather than relative to the floor of the experimental facility was done to ensure that the flame height measurements did not appear to artificially change due to the change in fuel bed height. The points on the top edge were located in a similar fashion as to how the points on the front edge were located for the flame front. However, in the case of flame height, the search was conducted along the columns of pixels in the binary image to find the top-most "true" location in each column. An outlier removal algorithm was used here in the same way as with the flame front points, however in this case outliers removed based on their distance from the median of points identified on the top of the flame. The median of the 10 highest points on the top of the

flame was taken to be the flame height (H) for each moment in time. A diagram showing the points identified on the top edge of the flame, shown in blue, and the resulting flame height, shown as a red line, is shown in Figure 3.4.

The mean flame height as a function of time for each fuel loading was then calculated using Equation 3.1 with $X = H$. The 95% confidence interval was then calculated using Equation 3.4.

For each test, the mean flame height for the entire test, $\overline{H}_i$, was taken as the mean of all flame height measurements taken during the steady-state region of that test. Next, the mean flame height for each fuel loading was calculated by taking the mean of the individual mean intensities for each test within a given fuel loading group using Equation 3.5 with $X = \overline{H}$. The 95% confidence interval of the mean intensity for each fuel loading was calculated using Equation 3.8.

3.7.5 Camera Calibration

In order to provide quantitative flame geometry measurements in world units (meters) rather than pixels, the camera was calibrated using a checkerboard calibration technique. A series of 12 images of a checkerboard pattern consisting of an 11 x 8 grid of 60 mm squares were used for the calibration. Figure 3.6 shows an example of one of the checkerboard calibration images. Since a checkerboard calibration of this type with a single camera can only be valid for the plane in which the checkerboard pattern was placed, the checkerboard was placed in the mid-plane of the width of the WildFIRE facility during calibration. The mid-plane was chosen so that the calibration would be most accurate in the middle of the width facility where the flame heights were observed to be maximum. In this way, the error on the flame height measurements could be minimized.

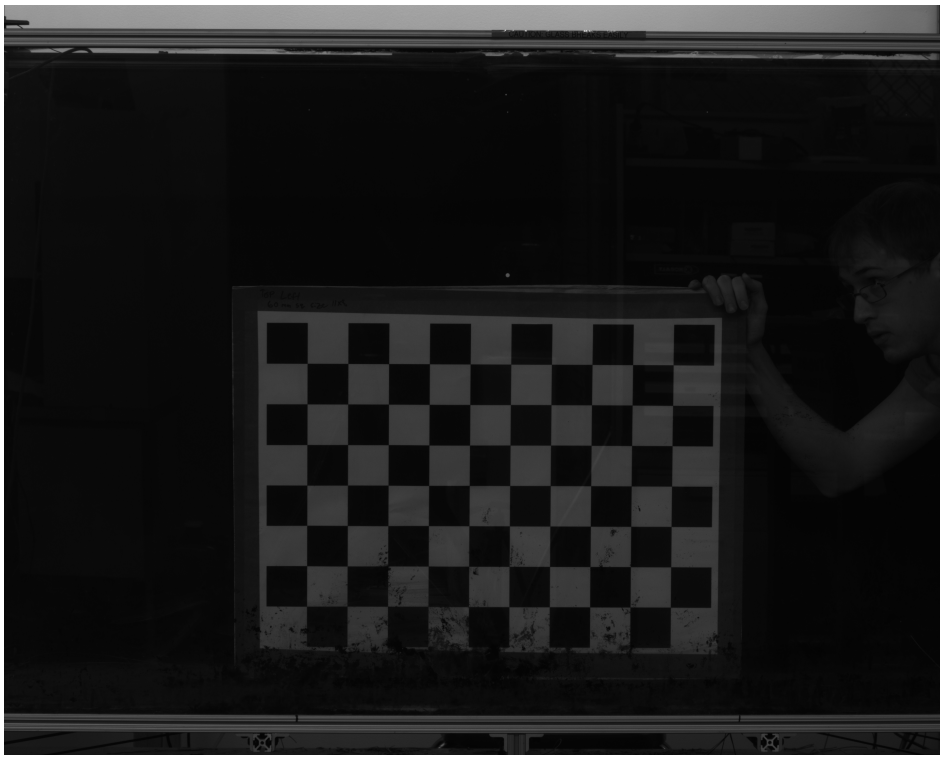

Figure 3.6: An example of one of the checkerboard calibration images taken to calibrate the flame geometry distance measurements.

Calibration factors at the near sidewall, mid-plane, and far sidewall of the WildFIRE facility were used to determine the amount of possible error should the maximum point on the flame exist at one of the extreme bounds of the facility rather than in the mid-plane where the calibration is valid. To assess this error, the flame height in world coordinates can be expressed in terms of pixel coordinates and a calibration factor as

$$H = \gamma y, \tag{3.16}$$

where H is the flame height in world units, γ is the calibration factor, and y is the flame height measured as pixels in the image coordinate system. Three calibration factors were then calculated. The first from an image of the ruler placed on the clear glass side wall of the facility nearest to the camera, γ_{near}, and the second from an image with ruler placed against the solid side-wall of the facility farthest from the camera, γ_{far}. Due to the angular field of view of the camera, the mid-plane calibration factor, γ_{mid}, can be calculated as the average of the near and far calibration

factors. These calibration factors can be used to estimate the maximum error since it is known that the flame must exist somewhere within the depth of the WildFIRE facility. Since the mid-plane calibration factor was the one used to convert the image coordinates into world coordinates, the maximum error of the flame height would occur if the maximum flame height actually existed at the near or far bound of the facility, rather than in the mid-plane. Based on this fact, the maximum absolute error in flame height was estimated as

$$\text{Error} = y|\gamma_{\text{mid}} - \gamma_{\text{near}}|. \tag{3.17}$$

Since the maximum flame height error is a function of the flame height, it is more useful to think of the error in terms of a percentage. The percent error of the flame height measurement can then be estimated as

$$\%\text{Error} = \frac{|\gamma_{\text{mid}} - \gamma_{\text{near}}|}{\gamma_{\text{mid}}} \times 100. \tag{3.18}$$

Using this equation, the flame height error was found to be $\pm 5.5\%$ of the reported value. In fact, it is likely that the error is typically lower than this since the maximum flame height has been observed to exist in or near the mid-plane of the facility.

Chapter 4

Results and Discussion

The results from this study are presented and discussed below. These results not only enhance the general understanding of the wildland fire burning characteristics of loblolly pine straw, but provide critical data for use in validating computational models to predict the spread of wildland fires. The fuel mass consumption rate, fire propagation rate, fire temperature, flame intensity, and flame geometry measurements presented here provide a multifaceted analysis regarding the burning characteristics of loblolly pine straw.

4.1 Mass Consumption Rate

This section presents the mass consumption rate results for the three fuel loadings tested of 0.98, 1.31, and 1.63 $\mathrm{kg/m^2}$. Loblolly pine straw with a nominal moisture content of 10% by mass was used to form a fuel bed with a bulk density of 20.6 $\mathrm{kg/m^3}$ for all tests. The fuel was ignited at one end of the burning surface using an alcohol soaked string to ensure simultaneous ignition across the width of the fuel bed as previously described. Once ignited, the fire was allowed to propagate until it reached the other end of the burning surface. Ten tests were conducted at each initial fuel loading to gain insight into the repeatability of the results. In the subsequent figures, the solid line is used to denote the mean value across the ten tests at each fuel loading as calculated using Equation 3.1. The the shaded region shows the 95% confidence interval across these ten tests as calculated using Equation 3.4.

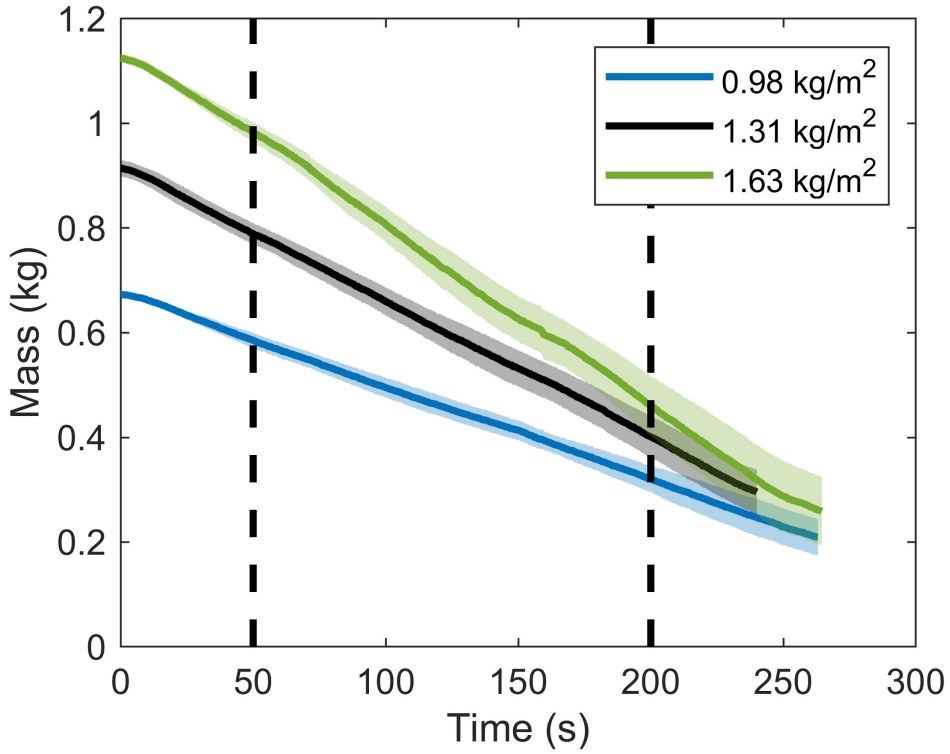

Figure 4.1: Time history of fuel mass for a range of initial fuel loadings. The solid line and shaded region represent the mean and 95% confidence interval, respectively, across ten tests at each fuel loading. The vertical dashed lines denote the steady-state region.

Figure 4.1 shows the fuel mass versus time for the initial fuel loadings tested. In the mass loss data, a slight increase in confidence interval over time was seen due to variations in the burning rate between individual tests within each fuel loading group. Due to these variations, the mass loss curves across the tests diverge slightly over time. This result was expected since the pine needle bed is not a homogeneous fuel, which means that while the tests were made as consistent as possible, the fuel bed properties around their nominal value result in no two fuel beds being identical.

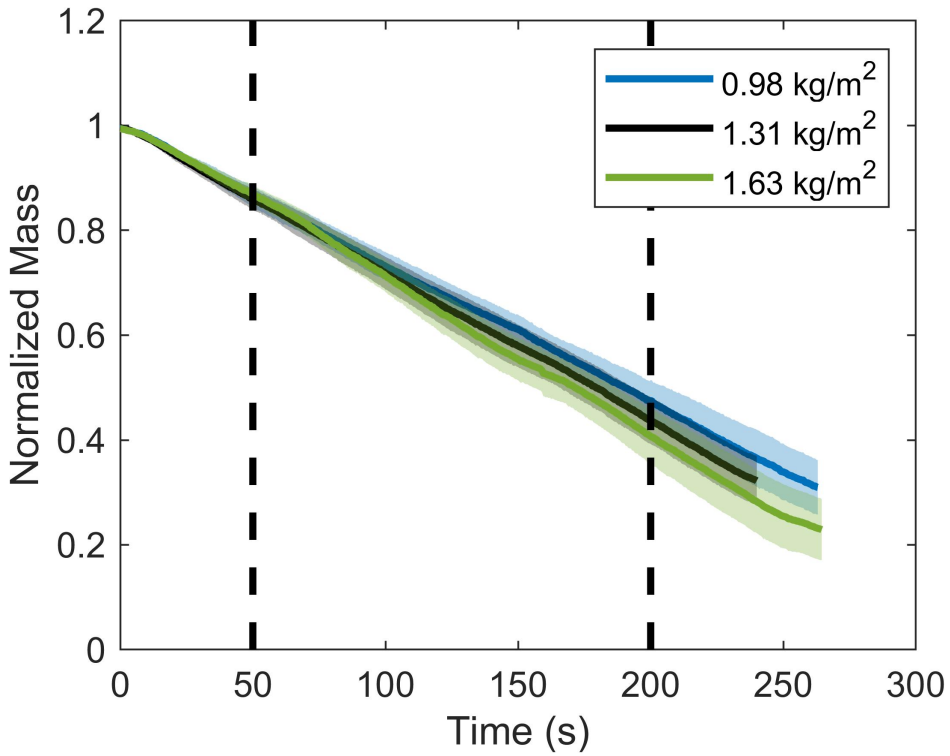

Figure 4.2: Time history of normalized fuel mass for a range of initial fuel loadings. The solid line and and shaded region represent the mean and 95% confidence interval, respectively, across ten tests at each fuel loading.

The mass loss behavior was found to be very linear. This is corroborated by the normalized mass results shown in Figure 4.2 where the fuel mass measurement at each point in time was normalized by the initial fuel mass for that test. The normalized mass loss curves collapse together having approximately the same slope. This indicates the relationship between the mass loss rate and the initial fuel loading is linear. Since bulk density, fuel bed length, and fuel bed width were held constant across the tests, increases in fuel mass resulted in increases in fuel bed height (shown in Table 3.1). This increase in fuel bed height results in more fuel available to be burned per unit length of the fuel bed.

As described in section 4.1, the fuel burn rate for each test was calculated by the slope of a linear-best fit from the mass loss data through the steady-state region of 50 to 200 s, which is denoted by the vertical black dashed lines in Figure 4.1. The calculated burn rates for each fuel loading are shown in Figure 4.3 and tabulated in Table 4.1. Burn rate was found to increase

linearly with increased fuel loading. A linear fit was applied to the mean burn rate results as a function of fuel loading. From the linear fit, it was found that the mean burn rate increased at a rate of 2.67E-3 $\mathrm{kg/s}$ for a 1 $\mathrm{kg/m^2}$ increase in fuel loading. The linear increase in burn rate with fuel loading suggests that the burn rate essentially scales itself as fuel loading increases such that the propagation rate along the length of the fuel bed remains nearly the same the same. Since the propagation rate does not significantly change, and more fuel is available for burning per unit length of the fuel bed with increased loading, it is natural that the mass loss rate must increase. This will be further discussed with the optically tracked flame front propagation results presented later.

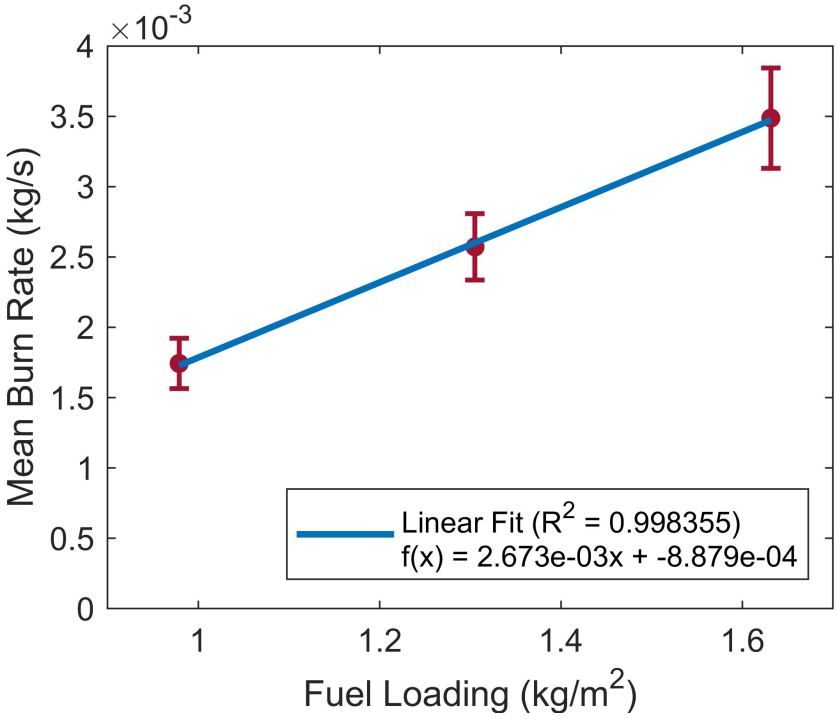

Figure 4.3: Mean burn rate versus initial fuel loading for a range of fuel loadings. Error bars denote the 95% confidence interval.

Table 4.1: Table of results from mass loss data. The 95% confidence interval is shown in parenthesis.

Fuel Loading ($\mathrm{kg/m^2}$)	Mean Burn Rate (g/s)	Normalized Mean Burn Rate (10^{-3})	Residual Mass Fraction
0.98	1.7 (0.18)	2.6 (0.26)	0.2327 (0.0404)
1.31	2.6 (0.24)	2.8 (0.24)	0.2233 (0.0546)
1.63	3.5 (0.36)	3.1 (0.30)	0.1771 (0.0349)

In addition to the mass loss rate, the consumption efficiency of the fire was also investigated. Consumption efficiency is an important wildland fire characteristic because it affects the efficacy of a prescribed burn and has a direct impact on the amount of harmful pollutants released from the fire. The consumption efficiency, in this case, was investigated via the residual mass fraction (η) defined in Equation 3.9. The mean residual mass fraction for each initial fuel loading is shown in Figure 4.4 and tabulated in Table 4.1.

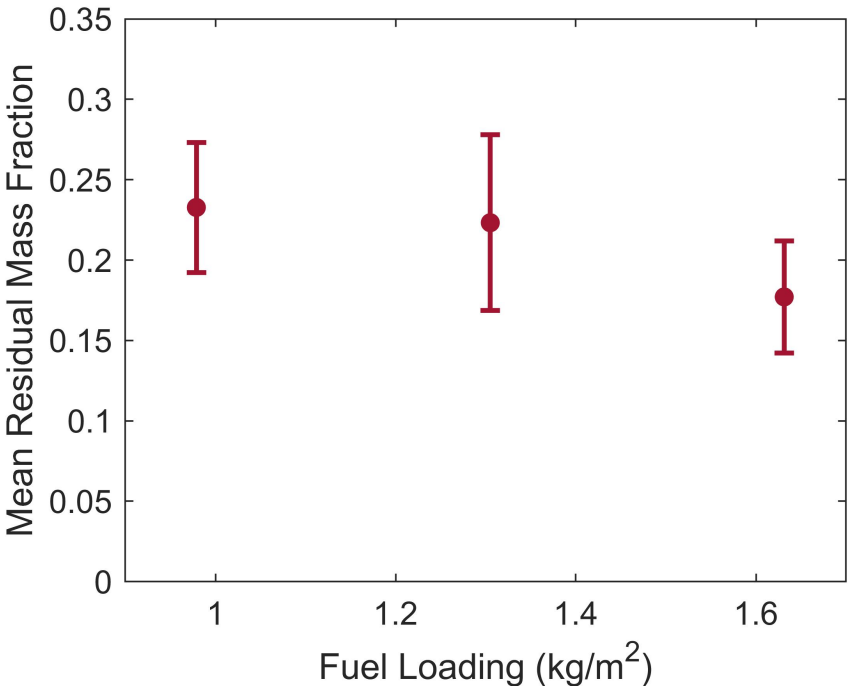

Figure 4.4: Mean residual mass fraction for a range of initial fuel loadings. Error bars denote the 95% confidence interval.

The residual mass fraction was found to decrease slightly over the range of fuel loadings tested. This decrease in residual mass fraction represents an increase in overall consumption efficiency and is likely due to the heat energy produced by the fire increasing with fuel loading, which results in more complete combustion of the fuel bed. At the lowest fuel loading value, the heat output from the fire was low enough that the combustion appeared to be at the lower limit of sustainable combustion. This resulted in areas of local extinction, which consequently resulted in some of the initial fuel remaining partially burned after the fire had passed. In fact, a lower fuel loading value of 0.65 $\mathrm{kg/m^2}$ was tested, and it was discovered that at this fuel loading the fire would sometimes extinguish before propagating through the entire length of the fuel bed.

The mass loss results show that as initial fuel loading was increased, so did the fuel mass consumption rate, and that this relationship between the initial fuel loading and the fuel mass consumption rate is strongly linear. Further investigation of the mass loss data showed that consumption efficiency increased across the range of fuel loadings studied. The temperature results

presented in the next section seek to provide further insight into the efficiency of the combustion process by investigating the effect that fuel loading has on the temperature of the fire.

4.2 Temperatures

The previous results discussed consumption efficiency as measured by the residual mass fraction and suggest that fuel loading and consumption efficiency are weakly linked. In traditional combustion analysis, combustion efficiency has been shown to be highly dependent on flame temperature [42]. In order to understand the effect of fuel loading on the temperature of the fire and what implications this might have for the combustion efficiency, an investigation into the effect of fuel loading on the temperature of the fire was conducted as described in section 3.5.

Figures 4.5 - 4.7 show the temperature as measured by the bottom, middle, and top thermocouples in the middle column, respectively. Due to the variation in time that the flame front reached the middle column of thermocouples from test to test, the data shown in these figures has been time shifted and trimmed such that the data starts at $t = 0$, which is defined as the point where the bottom thermocouple in the middle column first reaches a threshold temperature of 350 K. Doing this effectively simulates initiating the start of temperature data recording once the threshold temperature has been reached.

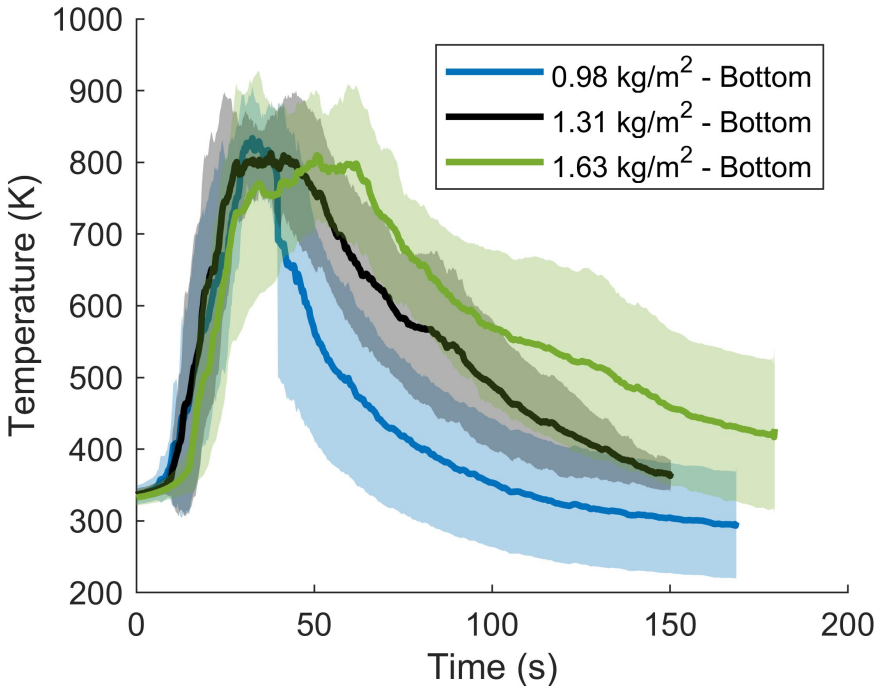

Figure 4.5: Time history of the flame temperature as measured by the bottom thermocouple in the middle column of thermocouples. The mean value averaged across the tests at each fuel loading is shown via the solid line and the 95% confidence interval is represented by the shaded region.

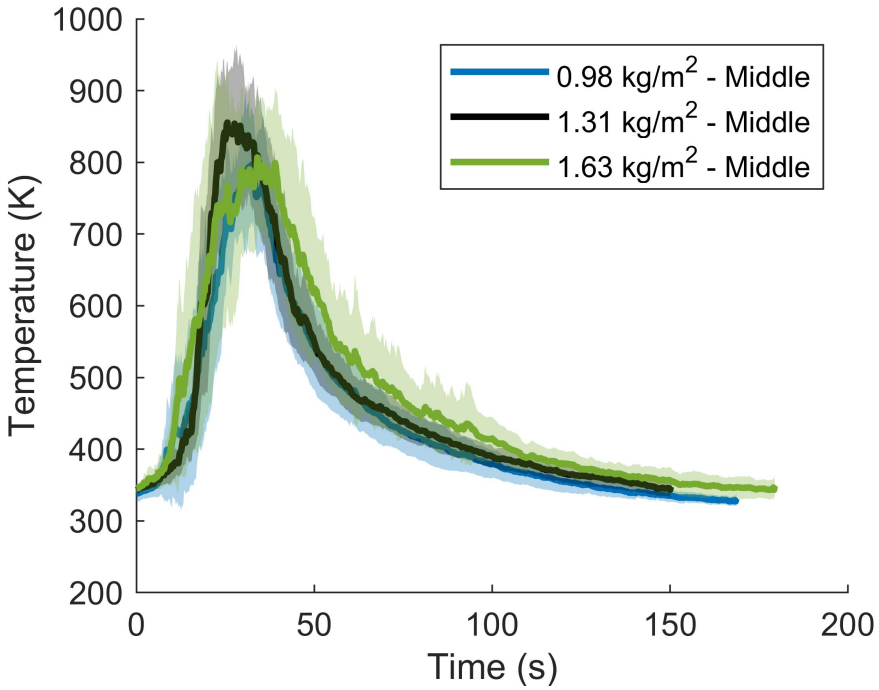

Figure 4.6: Time history of the flame temperature as measured by the middle thermocouple in the middle column of thermocouples. The mean value averaged across the tests at each fuel loading is shown via the solid line and the 95% confidence interval is represented by the shaded region.

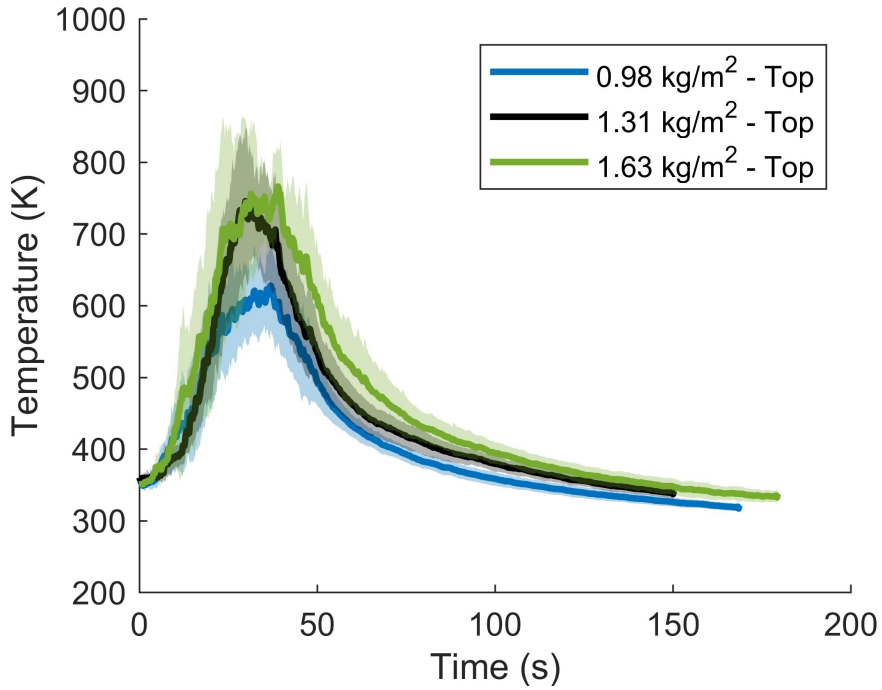

Figure 4.7: Time history of the flame temperature as measured by the top thermocouple in the middle column of thermocouples. The mean value averaged across the tests at each fuel loading is shown via the solid line and the 95% confidence interval is represented by the shaded region.

For all three thermocouple heights, the time history of the temperature data shows the flame front passing by the column of thermocouples as a relatively quick increase in temperature to a maximum value followed by a subsequent slower decrease as the flame front passes by. The decrease in temperature is slower than the initial increase due to secondary flaming combustion and smoldering fuel left behind the initial flame front. This is further evidenced by the fact that this slower decrease in temperature is more pronounced in the temperatures measured by the bottom thermocouple, which is placed in the fuel bed where the smoldering occurs. At the middle and top thermocouples, this slower decrease is still seen, but is not as notable due to the location of these thermocouples above the fuel bed. The temperatures measured by the bottom thermocouple during a time span of 50 to 175 s are noticeably higher for higher fuel loadings. This is likely due to the higher fuel loadings having a greater amount of smoldering fuel left behind the initial flame front.

This behavior is not seen by the middle and top thermocouples as they are not positioned within the fuel bed.

To further investigate the temperature data, the mean maximum flame temperature is shown for three relative heights within the flame at each of the fuel loadings tested in Figure 4.8 and tabulated in Table 4.2. The error bars shown at the top of each bar represent the 95% confidence interval of the maximum temperature for the ten tests at each fuel loading. The thermocouples were placed in the facility as shown in Figure 3.3 with the bottom, middle, and top rows of thermocouples being placed at 4.45, 14.45, and 24.45 cm above the floor of the facility, respectively. Using the fuel bed height and the measured mean flame height (presented in the next section), the location of the thermocouples was calculated relative to the mean flame height. The thermocouple locations relative to the mean flame height are tabulated in Table 4.3

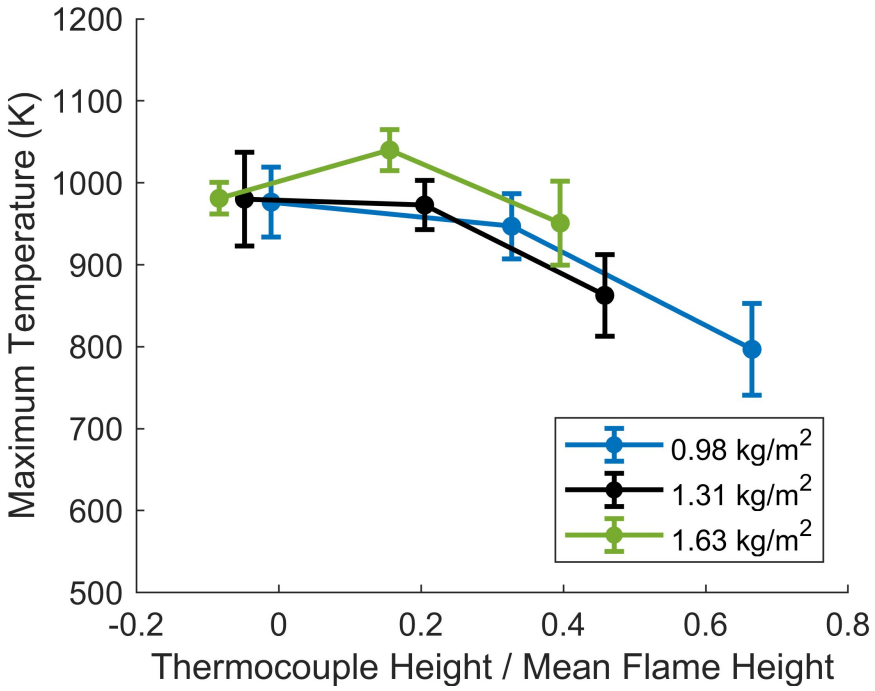

Figure 4.8: Maximum flame temperature as a function of relative location within the flame height for the range of initial fuel loadings. Error bars denote the 95% confidence interval.

Table 4.2: Maximum flame temperature at each height for the three initial fuel loadings tested. The 95% confidence interval is shown in parenthesis.

Fuel Loading ($\mathrm{kg/m^2}$)	Top (K)	Middle (K)	Bottom (K)
0.98	797 (55.8)	947 (39.9)	977 (42.6)
1.31	863 (49.8)	973 (30.0)	980 (57.2)
1.63	951 (51.4)	1004 (25.1)	981 (19.3)

Table 4.3: Relative thermocouple locations reported as fraction of total flame height. Negative values indicate that the thermocouple is located in the fuel bed, beneath the bottom of the flaming combustion zone.

Fuel Loading ($\mathrm{kg/m^2}$)	Top	Middle	Bottom
0.98	0.50	0.25	-0.01
1.31	0.45	0.20	-0.05
1.63	0.40	0.16	-0.08

The maximum measured temperature was found to increase with fuel loading and decrease with height within the flame. The increase in temperature with fuel loading was most pronounced for the top row of thermocouples. The increase in temperature was less pronounced for the middle row of thermocouples and there was no significant increase in temperature for the bottom row of thermocouples. The bottom row of thermocouples was placed in the fuel bed. The fact that the temperature at the same relative flame height location did not change significantly across the fuel loadings tested suggests that the fuel loading does not having an affect on the actual flame temperature of the fire. Rather, the flame temperature is most likely driven by the chemical kinetics properties of the pine needles. This is expected since wildland fire flames are buoyant diffusion flames from a solid fuel. As such, the combustion is taking place at stiochiometric conditions,

and therefore the flame temperature would not be expected to change with fuel loading. In other words, the fuel loading is not changing the underlying combustion reaction of loblolly pine straw. Instead, the fuel loading is affecting the size of the fire and other macroscopic properties such as flame height. The decrease in flame temperature with height in the flame is likely due to air mixing into the flame.

The mass loss and temperature measurements presented above provide valuable insight, but they do not provide the entire picture. For instance, it was found that the fuel mass consumption rate increases with initial fuel loading, but the mass loss data provides no direct information regarding the effect this has on the propagation rate of the flame front. Additionally, optical diagnostics are relatively simple to setup in the field compared to traditional diagnostic techniques such as load cells and thermocouples. The optical diagnostic results presented in the next section seek to provide further insight into the burning characteristics discussed so far and to provide a more comprehensive picture of the burning characteristics of loblolly pine straw overall.

4.3 Optical Diagnostic Results

Optical diagnostic techniques were used as described in section 3.7 to programmatically and non-intrusively measure the fire propagation, flame height, flame length, flame surface area, and flame intensity. These characteristics of the fire cannot be easily measured using traditional diagnostics such as load cells and thermocouples and provide valuable insight into the behavior of the fire.

4.3.1 Flame Front Propagation Rate

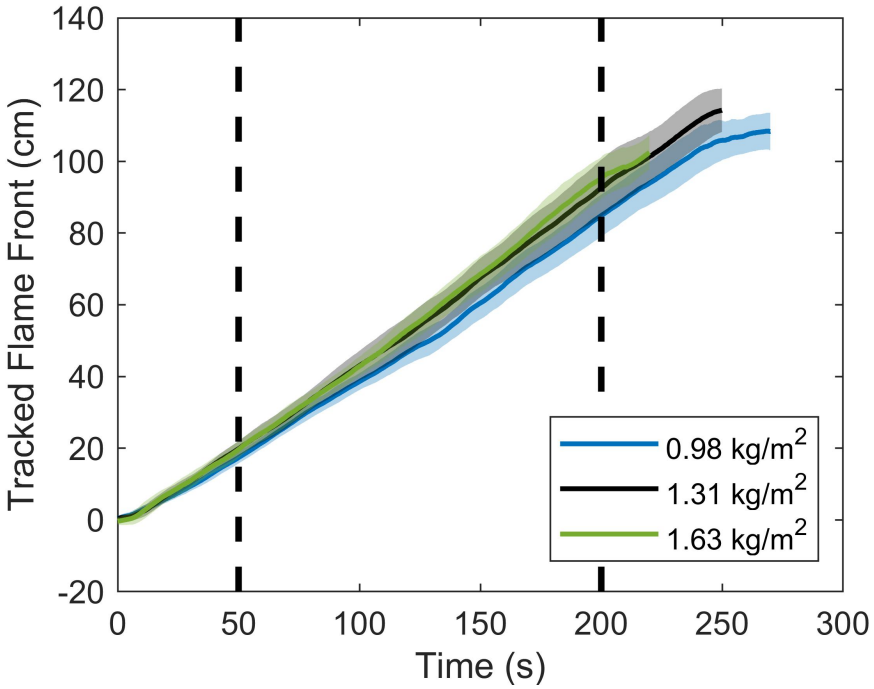

Figure 4.9: Optically tracked flame front for a range of initial fuel loadings. The solid line and shaded region represent the mean and 95% confidence interval, respectively, across ten tests at each fuel loading.

Figure 4.9 shows the optically tracked flame front location over time for a range of initial fuel loadings. From the optically tracked flame front results, the average fire propagation rate was calculated by applying a linear curve fit to the flame front versus time data recorded for each test. The linear curve fit was only applied to the the steady-state data range denoted by the two vertical dashed lines at 50 and 200 s. The average propagation rates for each test were taken to be the slope of these linear curve fits. The mean propagation rate for each fuel loading was calculated as the mean of the propagation rates for each of the ten tests at each fuel loading.

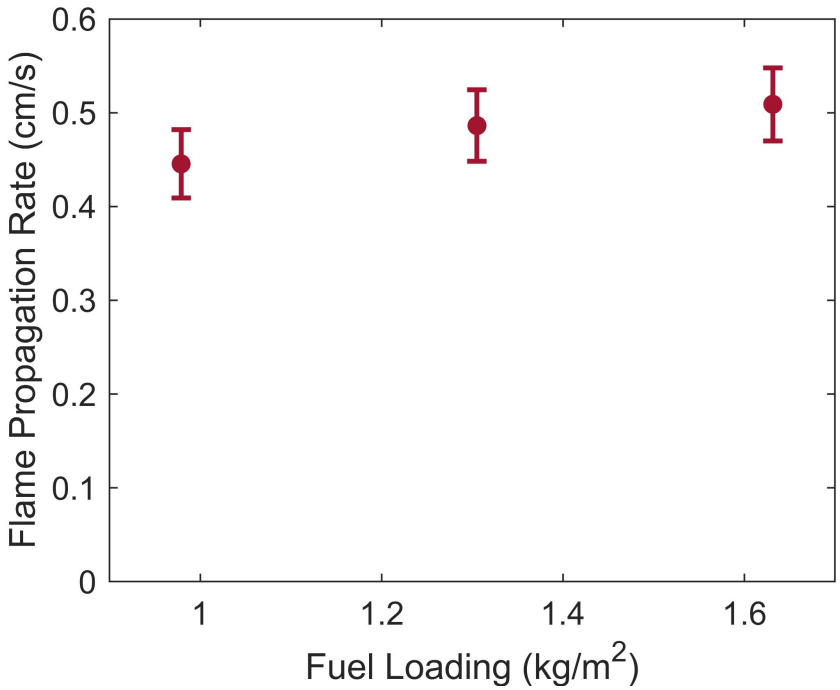

Figure 4.10: Propagation rate of the flame front as calculated from the optically tracked flame fronts for a range of initial fuel loadings. Error bars denote the 95% confidence interval.

The calculated propagation rate for each initial fuel loading is shown in Figure 4.10 and tabulated in Table 4.4. Each point uses error bars to represent the 95% confidence interval of the mean across the ten tests at each fuel loading. From these results, the propagation rate was found to increase slightly across the range of fuel loadings tested. Additionally, the propagation rate appears to be approaching some asymptotic value as the increase from the 0.98 $\mathrm{kg/m^2}$ to the 1.31 $\mathrm{kg/m^2}$ fuel loading is notably more than the increase from the 1.31 $\mathrm{kg/m^2}$ to the 1.63 $\mathrm{kg/m^2}$ fuel loading. This asymptotic increase in propagation rate with fuel loading has been seen in previous studies as well [20]. This increase in propagation rate with fuel loading could possibly be a result of the higher heat output from fires with higher fuel loadings. At lower fuel loadings relatively more of the energy output from the fire is required to pyrolyze and combust the fuel in the next unit length of the fuel bed compared to the heat output from higher fuel loadings. In fact, it is likely that as fuel loading continued to decrease, the propagation rate would slow until the point that the fire was no longer able to propagate through the fuel bed. With regards to the asymptotic

increase in propagation rate, it has been stated in the literature that the temperature in front of the fire front decreases exponentially [36]. As such, it is reasonable to conclude that the effects of increased heat output from higher fuel loadings would only be able to have a limited impact on pre-heating the fuel ahead of the flame front. The small change in propagation rate yet significant and linear change in mass loss rate indicates that the increase in mass loss rate is primarily due to the increased amount of fuel available to the fire per unit length of the fuel bed.

Table 4.4: Table of optically tracked fire propagation rate results. The 95% confidence interval is shown in parenthesis.

Fuel Loading ($\mathrm{kg/m^2}$)	Average Propagation Rate (cm/s)
0.98	0.4455 (0.0363)
1.31	0.4863 (0.0381)
1.63	0.5090 (0.0389)

To further investigate the relationship between the propagation rate and the mass loss rate, the mass loss rate was calculated from the propagation rate data and compared with the actual measured mass loss rate. To calculate the mass loss rate from the propagation rate data, it was assumed that the fuel bed was homogeneous and that the propagating flame front is infinitely thin, consuming all of the fuel per unit length of the fuel bed as it propagates along the length of the bed. Under these assumptions, the mass loss rate as calculated from the propagation rate would be

$$\dot{m}_{\mathrm{calc}} = \dot{L}_{\mathrm{meas}} \rho A_{\mathrm{CS}}, \tag{4.1}$$

where $\dot{m}_{\mathrm{calc}}$ is the mass loss rate calculated from the propagation rate, $\dot{L}_{\mathrm{meas}}$ is the propagation rate measured from the optically tracked flame front, ρ is the bulk density of the fuel, and A_{CS} is the width-wise cross-sectional area of the fuel bed. The bulk density represents the mass of fuel

per unit volume of the fuel bed as

$$\rho = \frac{m_o}{L_{\mathrm{FB}} W_{\mathrm{FB}} H_{\mathrm{FB}}}, \tag{4.2}$$

where L_{FB}, W_{FB}, and H_{FB} are the length, width, and height of the fuel bed respectively. The width-wise cross-sectional area is then

$$A_{\mathrm{CS}} = W_{\mathrm{FB}} H_{\mathrm{FB}}. \tag{4.3}$$

Substituting Equations 4.2 and 4.3 into Equation 4.1 yields

$$\dot{m}_{\mathrm{calc}} = \dot{L}_{\mathrm{meas}} \frac{m_o}{L_{\mathrm{FB}}}, \tag{4.4}$$

which was used to calculate the mass loss rate from the optically measured propagation rate. This equation would be valid if the entirety of the fuel mass was burned in the fire, but it is known that this is not the case from the residual mass fraction results. Therefore, Equation 4.4 is corrected to consider the residual mass fraction by replacing m_o with $m_b = m_o - m_f$, where m_b is the mass of fuel actually burned and m_f is the mass remaining after the fire has extinguished. The calculated mass loss rate then becomes

$$\dot{m}_{\mathrm{calc}} = \dot{L}_{\mathrm{meas}} \frac{m_b}{L_{\mathrm{FB}}}. \tag{4.5}$$

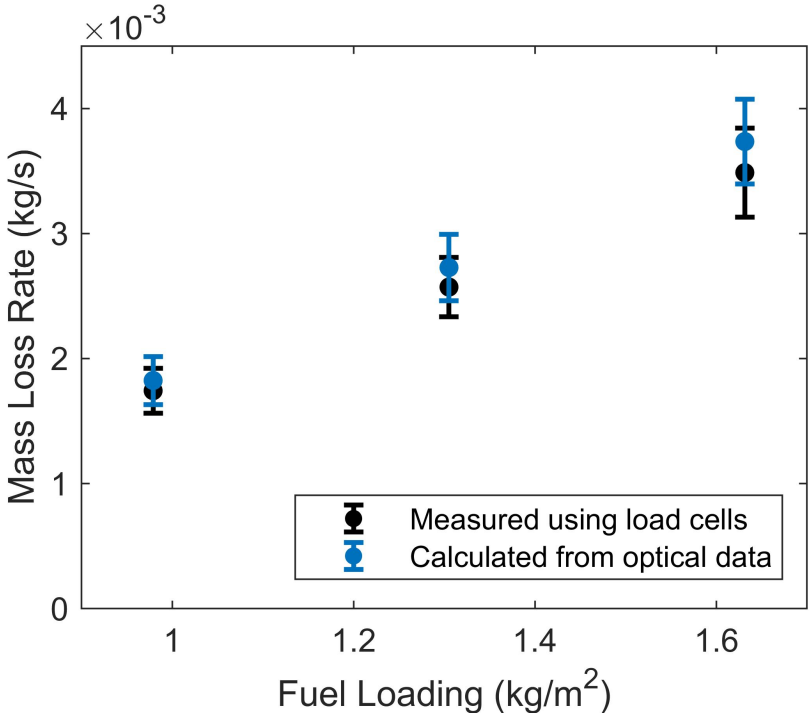

Figure 4.11: Comparison of the mass loss rate measured using load cells with the mass loss rate calculated from the optically tracked flame front propagation. The error bars denote the 95% confidence interval.

The mass loss rate calculated from the optically measured propagation data is shown in Figure 4.11 for the range of fuel loadings tested. The values were found to be in good agreement suggesting that the majority of the mass loss rate is a result of flaming combustion occurring within a relatively thin flaming region that propagates along the length of the fuel bed rather than from smoldering or secondary flaming combustion that exists after the primary flame front has passed. However, as fuel loading increased, so did the difference between the actual measured mass loss rate and the mass loss rate as calculated from the flame propagation data. The mass loss rate calculated from the propagation data began to over-estimate the actual mass loss rate to an increasing extent with increased fuel loading. This is likely due to the thicker fuel beds at higher fuel loadings resulting in more secondary combustion behind the primary flame front burning downwards through the height of the fuel bed while the primary flame front continues on propagating along

the top of the fuel bed. This will be further discussed in the section presenting the flame length results.

It is also possible to calculate the propagation rate from the measured mass loss data. This was done in similar form to Equation 4.5 solving instead for $\dot{L}_{\mathrm{calc}}$ from $\dot{m}_{\mathrm{meas}}$as

$$\dot{L}_{\mathrm{calc}} = \frac{\dot{m}_{\mathrm{meas}}}{m_b / L_{\mathrm{FB}}}, \tag{4.6}$$

where $\dot{m}_{\mathrm{meas}}$ is the mass loss rate as measured directly from the mass loss data. The propagation rate calculated from the measured mass loss data is shown and compared with the optically measured propagation rate in Figure 4.12. Calculating the flame front propagation rate in this way results in an under-estimation when compared to the actual measured propagation. This is again because the the calculation performed using Equation 4.6 assumes all of the mass consumed is consumed via flaming combustion. This assumption was shown by the previous results to become increasingly invalid as fuel loading is increased due, presumably, to an increasing amount of secondary and smoldering combustion continuing behind the flame front and burning through the depth of the fuel bed. Despite this, the agreement between the two methods of fairly good, suggesting that optically measured propagation rate could potentially be used to estimate mass loss rate, especially if some empirical function were used taking into account the increase in secondary combustion. Such a relation could perhaps be taken one step further and used to estimate heat release rate, since it has already been demonstrated in the literature that heat release rate can be reasonably estimated from mass loss rate [18]. Further testing would be required to fully develop this relationship, and such testing was beyond the scope of the present work.

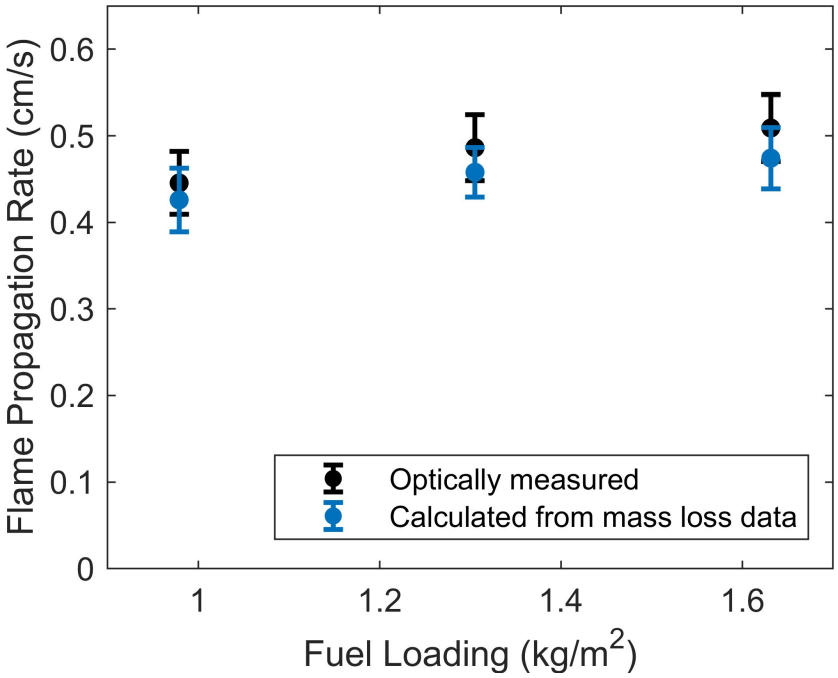

Figure 4.12: Comparison of the propagation rate measured from the optically tracked flame front compared with the propagation rate calculated from the mass loss data. The error bars denote the 95% confidence interval.

4.3.2 Flame Height

As described in section 3.7, the flame height was extracted from the optical diagnostics data. Understanding the behavior of the flame height is important for understanding how the fuel loading affects the manner in which the fire behaves and spreads. For instance, a taller flame is more prone to igniting low hanging tree branches which could result in the fire spreading into the tree canopy. The flame height measurements are presented and discussed in the paragraphs below.

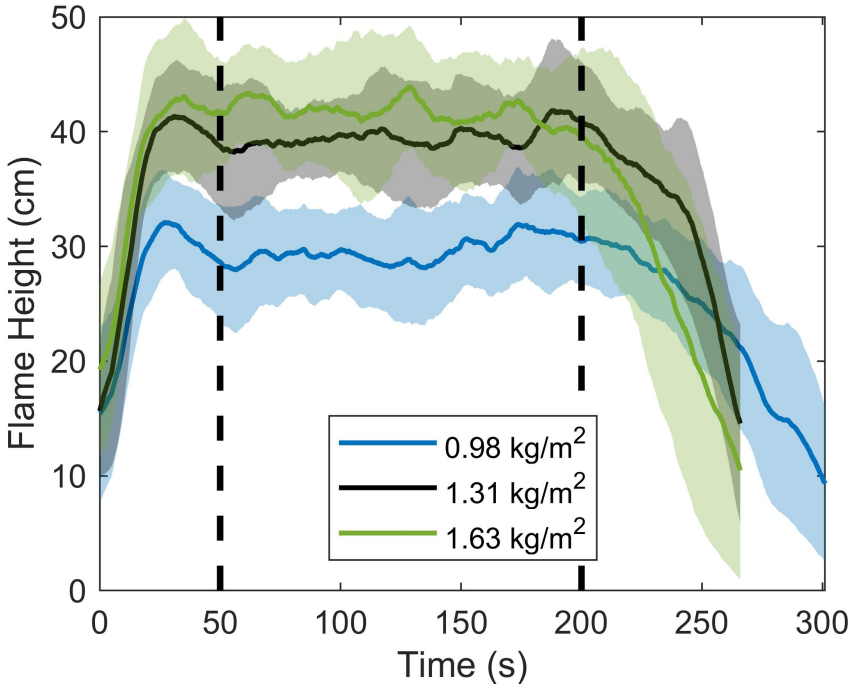

Figure 4.13: Flame height versus time for a range of initial fuel loadings. The solid line and shaded region represent the mean and 95% confidence interval, respectively, across ten tests at each fuel loading. The dashed lines denote the steady-state region.

The flame height over time for the three initial fuel loadings studied is shown in Figure 4.13. The flame height for all fuel loadings starts low and and increases over the first 50 s until reaching a quasi steady-state, where it remains until tapering downwards as the burn concludes at around 200 s. The initial buildup in the flame height at the beginning of the burn is due to the flame starting initially small from the alcohol soaked string used as the source of ignition and then increasing in size as the fire grows in strength and spreads to neighboring fuel. Similarly, the decrease in flame height at the end of the test is due to the flame extinguishing as it reaches the end of fuel available for burning. Outside of the startup and shutdown transients seen, flame height generally appears stable around a given mean value.

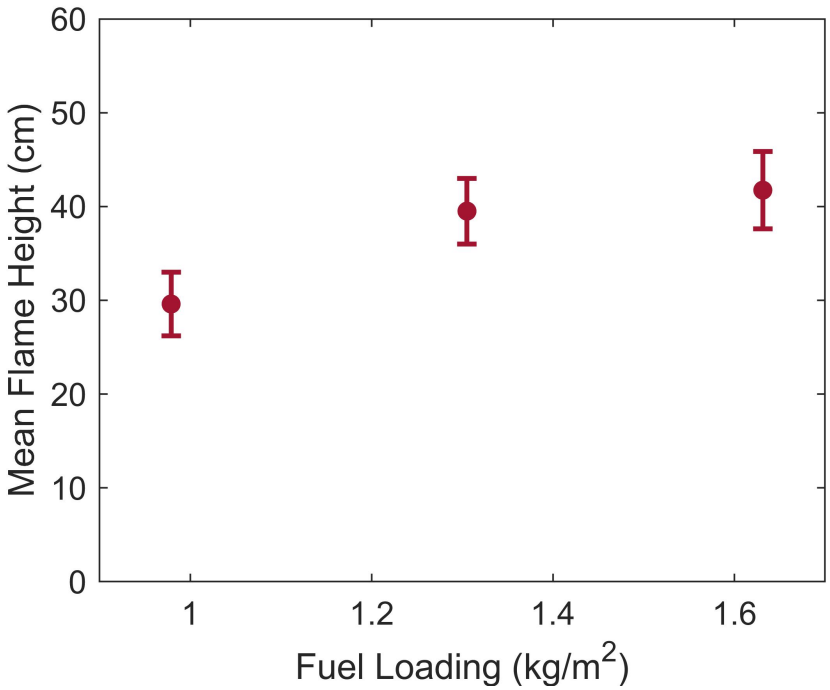

Figure 4.14: Mean flame height for a range of initial fuel loadings. Error bars denote the 95% confidence interval.

The mean flame height for each fuel loading was calculated by taking the mean of the flame height during the steady-state time of the burn and is shown in Figure 4.14 and tabulated in Table 4.5. The mean was restricted to the steady-state region of 50 to 200 s, represented by the dashed black lines in Figure 4.13, to prevent transients at the beginning and end of the burns from affecting the result. The mean flame height was found to increase with fuel loading, and appeared to be reaching an asymptotic value of approximately 45 cm. This increase of flame height with fuel loading has been seen by previous studies [14, 20]. The increase in flame height is likely due to the increased amount of fuel available per unit length of the fuel bed. As such, more fuel is being combusted at any point in time, which we have seen in the case of the mass loss rate results. Since more fuel is being combusted, it is only natural that the height of the flame would increase to consume the larger amount of pyrolyzed fuel gasses being released. It also is important to note that the flame height was measured from the images taken through the CH* band-pass filter. As such, the reported flame height is the height of the actual heat release region of the flame. Because

of this, the increase in flame height shown here also indicates the heat release region of the flame is increasing. This will be further discussed in the flame surface area results.

Table 4.5: Table of optically tracked flame height results. The 95% confidence interval is shown in parenthesis.

Fuel Loading ($\mathrm{kg/m^2}$)	Mean Flame Height (cm)
0.98	29.6 (3.40)
1.31	39.5 (3.49)
1.63	41.7 (4.13)

4.3.3 Flame Length

In addition to flame height, the flame length was also extracted from the optical diagnostics data. Flame length in this case was defined as the distance from the rearward-most edge of the flame to the forward-most edge of the flame. As such, larger flame lengths would indicate that the fire is burning quickly over the top of the fuel bed leaving lingering flames behind that continue to consume through the height of the fuel bed. By contrast, small flame lengths would indicate a relatively thin flame front propagating along the fuel bed and consuming much of its thickness at once, leaving only smoldering embers in its path.

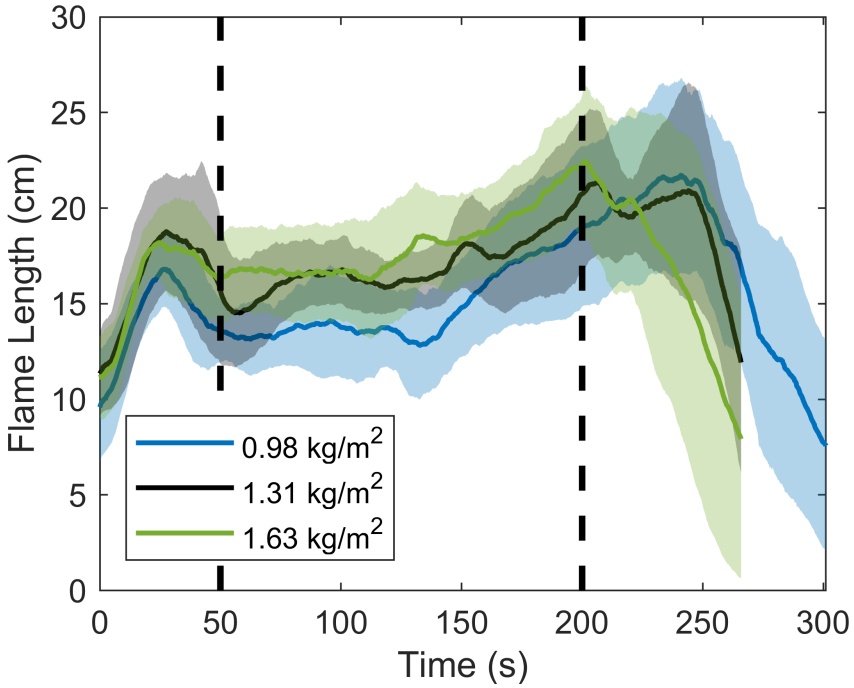

Figure 4.15: Flame length versus time for a range of initial fuel loadings. The solid line represents the mean across three tests at each fuel loading and the shaded region represents the 95% confidence interval.

The flame length starts low, at around 10 cm, before increasing to a value of approximately 20 cm and then decreasing back to value of approximately 15 cm. This initial rise and subsequent decrease is an artifact of the way the fire was ignited. When the alcohol soaked string is lit, the flame front immediately begins to propagate along the length of the fuel bed, but the alcohol soaked string continues to burn. During this time, the propagating flame front represents the forward-most edge of the flame and the alcohol soaked string represents the rearward-most edge. Once the alcohol soaked string extinguishes at around 50 s, this startup transient region is complete, and the flame length measurement becomes valid. The region during which the flame length measurement is taken to be valid is marked by the vertical dashed black lines in Figure 4.15.

During the valid region, the flame length was observed to steadily increase as the burn progressed for all three fuel loadings tested. Another way to interpret this result is that the forward-most edge of the flame is propagating at a rate slightly higher than the rearward-most edge. This

indicates that there are regions of smoldering and secondary combustion lingering behind the primary flame front. At the end of the steady-state region, a time of 200 s, the flame length was found to decrease again. This is due to the forward-most edge of the flame front reaching the farthest end of the fuel bed and extinguishing. The rearward-edge of the flaming combustion zone then continues to propagate, resulting in a decrease in flame length, until it also reaches the edge of the fuel bed and extinguishes.

The flame length was found to have a slight overall increase with fuel loading. This is likely due to the increased regions of secondary and smoldering combustion, mentioned previously, that continue to burn downwards through the height of the fuel bed behind the leading flame front. The increase in overall flame length with fuel loading appears to be relatively linear, potentially indicating that it is linearly related to the increase in fuel bed height. Since the flame length was not observed to be quasi-steady at any point during the test, no effort was made to calculate a mean flame length as a function of fuel loading.

4.3.4 Flame Area

The previous results outlining the flame height and length provide valuable insights into the burning behavior of the fire, perhaps the most useful way to leverage the flame images is to calculate the surface area of the flame as viewed from the camera. Since the camera was positioned to have a side-view of the flame, the surface area calculated here represents the surface area of the flame per unit width of the fuel bed.

The surface area of the flame was calculated using the number of pixels in each frame that were identified to be part of the flame. A calibration constant was then applied to convert this into real-world units of flame surface area. Figure 4.16 shows the flame surface area over time for the fuel loadings studied.

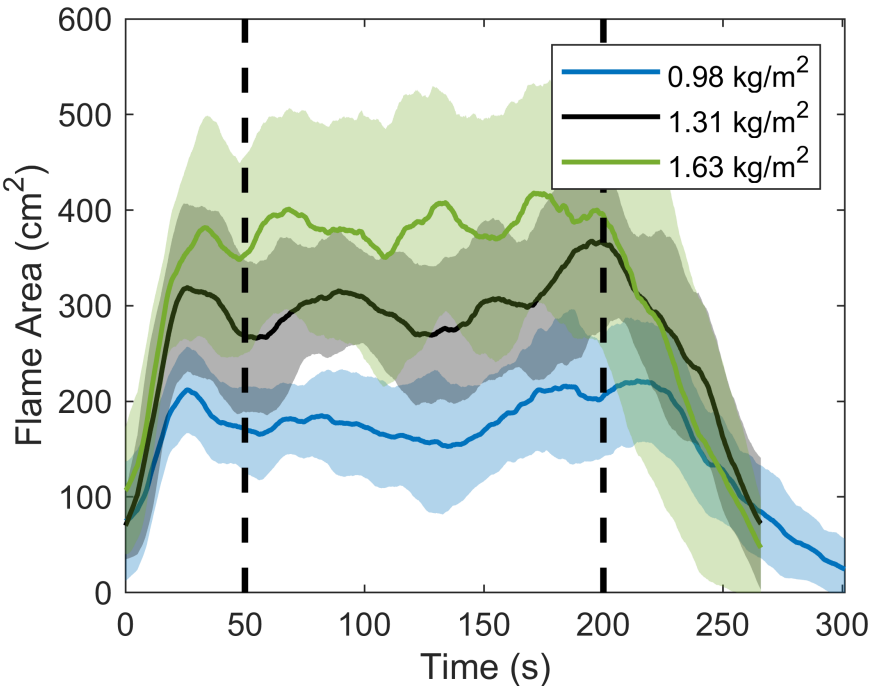

Figure 4.16: Flame area versus time for a range of initial fuel loadings. The solid line represents the mean across three tests at each fuel loading and the shaded region represents the 95% confidence interval.

Based on the results of the flame height and flame width, shown in Figures 4.13 and 4.15, respectively, the behavior of the flame area is not surprising. It is important to note the overall flame area increase with fuel loading seems to be resulting primarily from an increase in flame height.

As was done with the previous optically measured flame geometry properties, the mean flame surface area can also be plotted as a function of fuel loading by time averaging through the quasi-steady region of 50 to 200 s. The mean flame surface area versus fuel loading is shown in Figure 4.17 and tabulated in Table 4.6. From these results, it seems that the flame surface area increases almost linearly with fuel loading. There is a slight asymptotic decay that is likely a result of the asymptotic decay if flame height, however the effect is less than was seen in the flame height results. It is hypothesized that the increase in flame length with fuel loading is decreasing the impact of the asymptotic nature of the flame height increase. Further tests across a larger range

of fuel loadings would be required to test whether flame surface area is also approaching some maximum value.

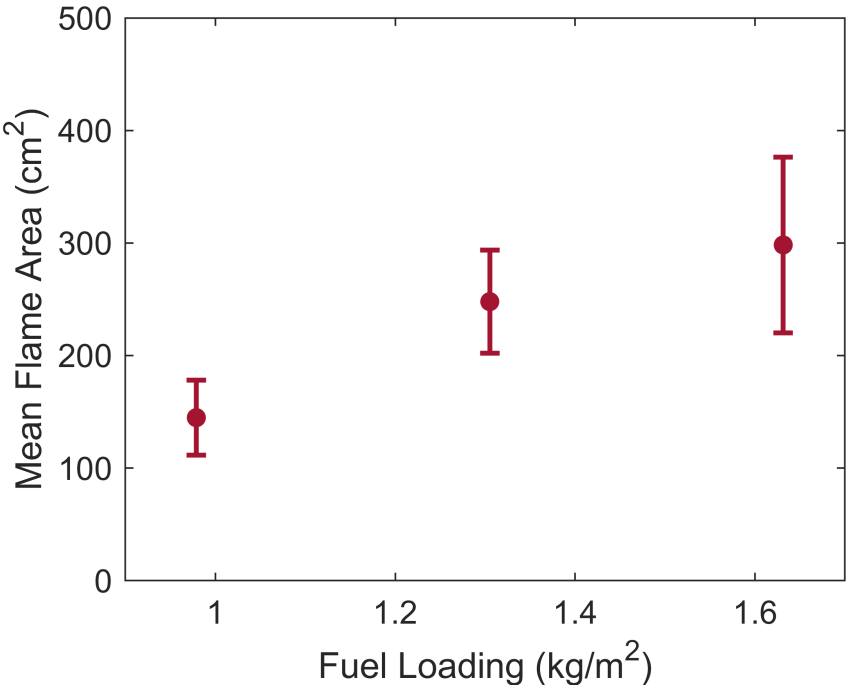

Figure 4.17: Flame area for a range of initial fuel loadings. Error bars denote the 95% confidence interval.

Table 4.6: Table of flame surface area results. The 95% confidence interval is shown in parenthesis.

Fuel Loading ($\mathrm{kg/m^2}$)	Flame Surface Area ($\mathrm{cm^2}$)
0.98	144.82 (33.48)
1.31	247.90 (45.74)
1.63	298.29 (78.14)

4.3.5 Flame Intensity

As described in detail section 3.7, flame intensity was extracted from the optical diagnostics data by summing the intensity value of each flame pixel in the image and then dividing by the number of flame pixels. As such the flame intensity shown here represents the flame intensity per unit area from the camera's perspective. Figure 4.18 shows the flame intensity through a CH* chemiluminescence filter for a range of initial fuel loadings. The intensity was only calculated for the steady-state region of the burn, from 50 to 200 s, because the small size of the flame at the beginning and end of the burn caused the intensity calculation to be poorly conditioned.

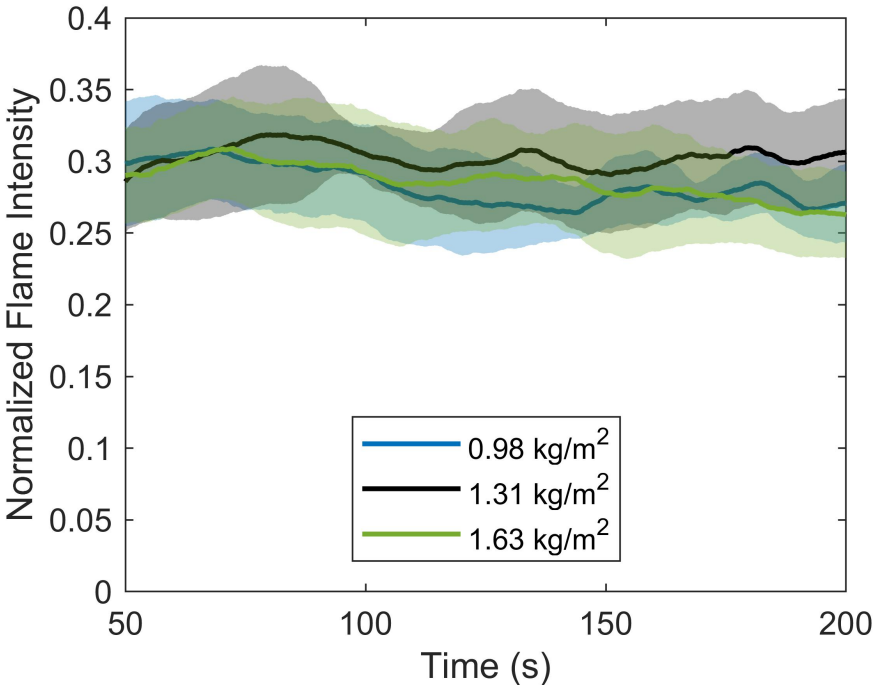

Figure 4.18: Normalized Flame intensity for a range of initial fuel loadings. The solid line and shaded region represent the mean and 95% confidence interval, respectively, across ten tests at each fuel loading.

The mean normalized flame intensity for each fuel loading was calculated and is shown in Figure 4.19 and tabulated in Table 4.7. From the flame intensity measurements, it was found that the flame intensity was not significantly affected by fuel loading. This is further evidenced by the fact that the maximum temperatures measured by the bottom and middle rows of thermocouples

also did not change significantly with fuel loading. As discussed in the temperature results section, this is not surprising since the gas-phase combustion process of loblolly pine straw is not likely to be changed by fuel loading. These two results together suggest that the intensity of the fire is driven by the chemical kinetic properties of the fuel rather than the physical arrangement of the needles within the fuel bed. Future tests should investigate the impact of bulk density on the burning intensity of the fire, but such tests were beyond the scope of this study.

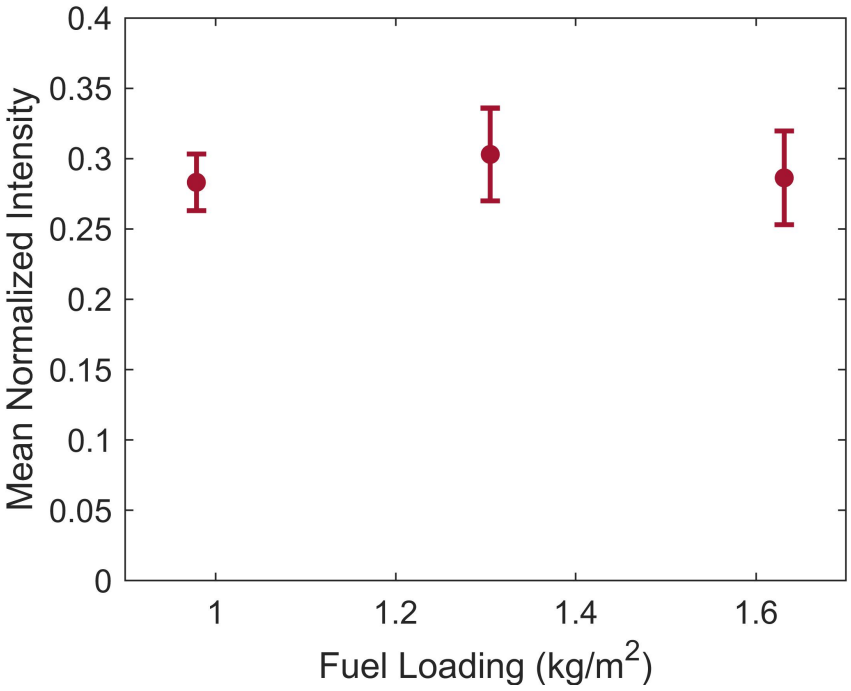

Figure 4.19: Flame intensity for a range of initial fuel loadings. Error bars denote the 95% confidence interval.

Table 4.7: Table of chemiluminescent flame intensity results. The 95% confidence interval is shown in parenthesis.

Fuel Loading ($\mathrm{kg/m^2}$)	Mean Normalized Flame Intensity
0.98	0.2831 (0.0200)
1.31	0.3030 (0.0331)
1.63	0.2863 (0.0332)

The fact that the flame intensity did not change significantly and the flame height increased with fuel loading indicates that while the heat release output per unit area of the fire is not increasing, the total heat output does simply due to a larger flame at the higher fuel loadings. This higher heat output is likely responsible for the reduction in residual mass fraction seen in section 4.1 and for the slight increase in propagation rate with fuel loading. Additionally, the fact that the intensity of the fire did not change significantly over the range of fuel loadings tested, but the burn rate did further suggests that the increase in burn rate is driven by the increase in available fuel per unit length rather than by an increase in the burning intensity of the fire. The flame height results corroborate this fact suggesting that the primary impact of increasing fuel loading is an increase in the amount of flaming combustion rather than an increase in the actual flaming intensity.

4.4 Emissions

Measurements of the concentrations of potentially harmful pollutants produced by the fire were recorded using a gas analyzer probe placed halfway along the length of the test section and at a height just above average flame heights such that it would sample pollutants being emitted from the fire. The average concentration of each pollutant was calculated by integrating the concentration over time for the entire test length and then dividing by the length of the test as shown in Equation 3.13.

Unfortunately, the emissions data presented in this section was taken when the gas analyzer was out of calibration. As such, the absolute values of emissions concentrations measured could not be trusted. For this reason, the emissions data presented in this section is shown on a relative scale where all values have been divided by the maximum average concentration measured across the fuel loadings. Doing this allows for comparing the relative emissions across fuel loading groups, without presenting absolute quantities that were potentially erroneous due to the gas analyzer being un-calibrated. Furthermore, the emissions data comprised only three tests at each fuel loading group. Because of this, the emissions data presented here is presented along with the standard error across the three tests at each fuel loading rather than the 95% confidence interval as was done for the other data.

Figures 4.20, 4.21, and 4.22 show the relative average concentrations of each CO, NOx, and SO_2, respectively, for the three initial fuel loadings tested.

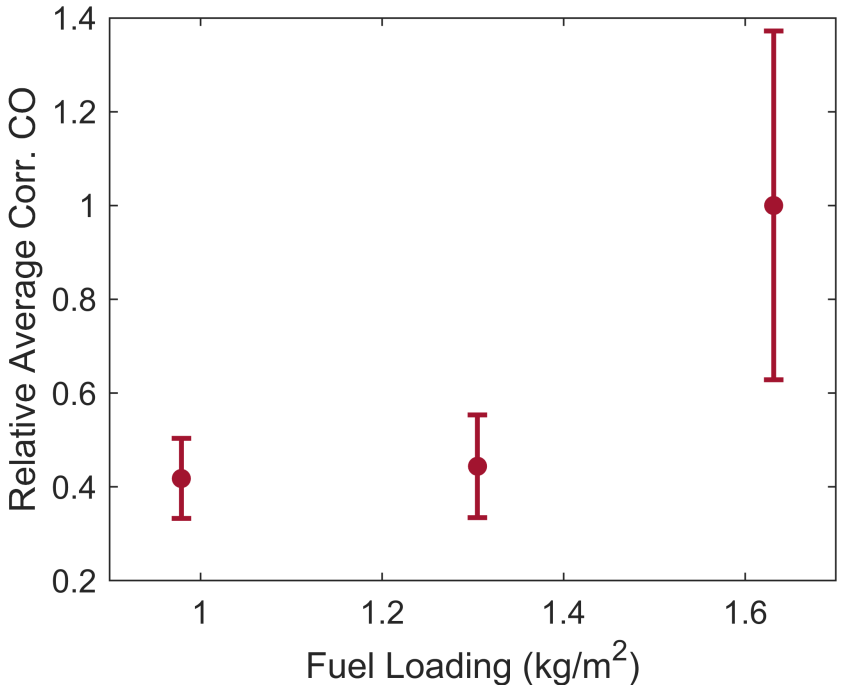

Figure 4.20: Relative average CO output for a range of initial fuel loadings. Error bars denote the standard error of the mean.

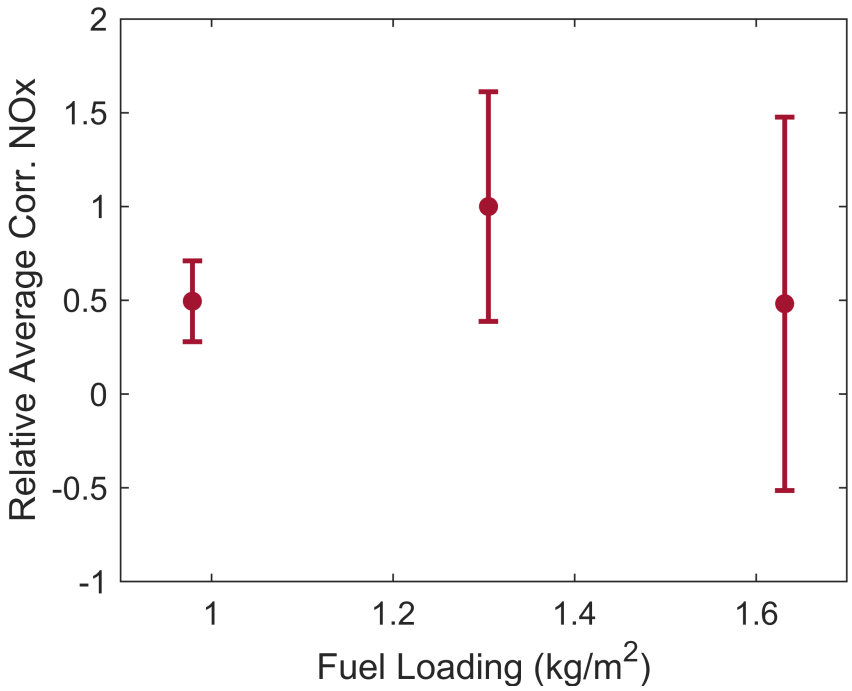

Figure 4.21: Relative average NOx output for a range of initial fuel loadings. Error bars denote the standard error of the mean.

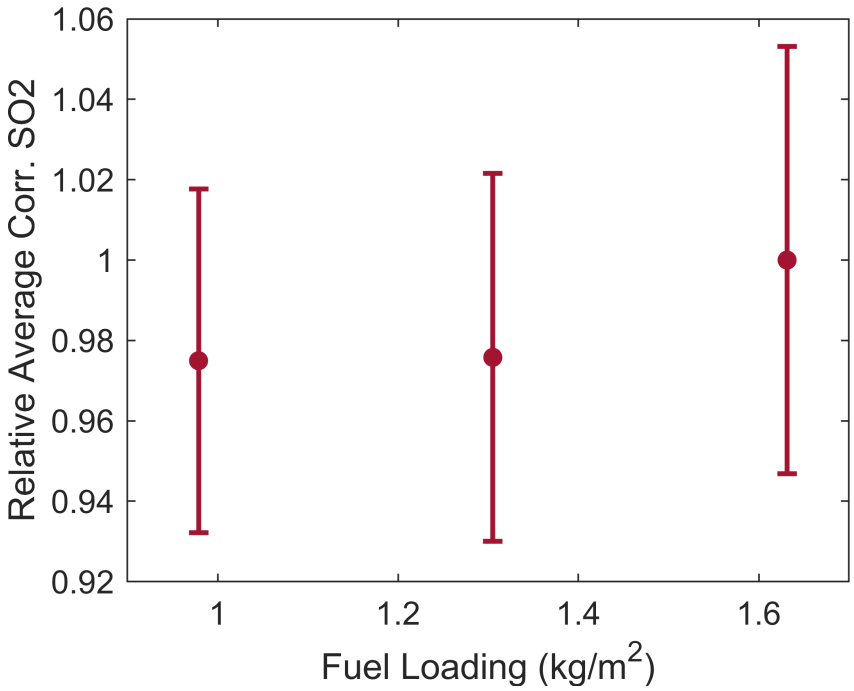

Figure 4.22: Relative average SO_2 output for a range of initial fuel loadings. Error bars denote the standard error of the mean.

It is important to understand the production of CO, NOx, and SO_2 from wildland fires as they are all harmful pollutants that have a negative impact on the environment. Carbon monoxide is commonly produced from incomplete combustion processes and is a harmful pollutant contributing to global warming. Nitrogen oxides are commonly produced from high temperature combustion reactions and are the cause for acid rain when they combine with sulfur dioxide in the atmosphere. It was found that the average CO concentration increased with fuel loading, which is likely attributed to an increased amount of fuel burning at any one moment in time. The NOx concentration remained very near zero with relatively large variations from test to test contributing to the large standard error. As such, the NOx results could not be considered significant. The average SO_2 concentration remained low, but shows a steady increasing trend across the range of fuel loadings tested. Table 4.8 shows the average concentrations of each measured pollutant along with the change in concentration found per unit increase in fuel loading as calculated via a linear regression technique. These results are expected from a wildland fire as the relatively low

flame temperatures result in incomplete combustion, which produces CO, and are not hot enough to support the reactions between nitrogen and oxygen, which would result in the creation of NOx.

Table 4.8: Table of pollutant species concentrations. The standard error is shown in parenthesis.

Fuel Loading ($\mathrm{kg/m^2}$)	CO (ppm)	NOx (ppm)	SO_2 (ppm)
0.98	0.4147 (0.0854)	0.4949 (0.2161)	0.9750 (0.0428)
1.31	0.4439 (0.1094)	1.0000 (0.6117)	0.9758 (0.0458)
1.63	1.0000 (0.3720)	0.4818 (0.9954)	1.0000 (0.0352)

The emissions data presented here can be used to assess how the various burning configurations affect pollution levels and inform future decisions on how best to conduct prescribed burns in addition to providing another valuable point of comparison for wildland fire modeling and simulation efforts.

4.5 Comparison with previous results

The results from this study can be compared with results from previous works that measured the burning characteristics of other types of pine needle beds in a similar facility. In particular, the studies by Dupuy [22] and Tihay et al. [20] are used. Dupuy studied 1 m by 1.5 m fuel beds of *Pinus pinaster* and *Pinus halepensis* needles with fuel loadings ranging from 0.4 to 1.2 $\mathrm{kg/m^3}$. Dupuy reported the *P. pinaster* to have a surface-area to volume ratio of 4550 $\mathrm{m^{-1}}$ and a density of 680 $\mathrm{kg/m^3}$. The *P. halepensis* beds were reported to have a surface-area to volume ratio of 10,420 $\mathrm{m^{-1}}$ and a density of 735 $\mathrm{kg/m^3}$. However, it should be noted that in a later study Dupuy et al. [24] note that the surface-area to volume ratio reported in [22] was likely over-estimated and that a more reasonable surface-area to volume ratio of the *P. halepensis* beds would be 7000 $\mathrm{m^{-1}}$. Dupuy reported the packing ratio of both beds to be approximately 0.03, which would place the

bulk density at 20.4 $\mathrm{kg/m^3}$ and 22.05 $\mathrm{kg/m^2}$ for the *P. pinaster* and *P. halepensis* beds, respectively. Tihay et al. studied 1 m by 2 m fuel beds of *P. pinaster* needles with fuel loadings of 0.6, 0.9, and 1.2 $\mathrm{kg/m^2}$ [20]. The reported surface-area to volume ratio and density were 3057 $\mathrm{m^{-1}}$ and 511 $\mathrm{kg/m^3}$, respectively. In the Tihay et al. study, the fuel bed depth changed with each fuel loading, resulting in slight changes in packing ratio and bulk density across the fuel loadings tested, but the nominal packing ratio was kept to 0.04.

The fuel beds used for the current study compare favorably in physical characteristics to the fuel beds used by Dupuy [22] and by Tihay et al. [20]. The bulk density and packing ratio of the current study were 20.5 $\mathrm{kg/m^3}$ and 0.04, respectively, and compare favorably to the values in the Dupuy and Tihay et al. studies. The fuel loadings tested of 0.98, 1.31, and 1.63 $\mathrm{kg/m^2}$ skew slightly higher than the fuel loadings tested by Dupuy and by Tihay et al., but still have good overlap. The surface-area to volume ratio of the *P. taeda* needles used in the present study was estimated to be 4000 $\mathrm{m^{-1}}$, which is most similar to the *P. pinaster* needles used in the Dupuy [22] study. Figures 4.23 and 4.24 show the measures mass loss rate and propagation rate compared to results from the Dupuy [22] and the Tihay et al. [20] studies.

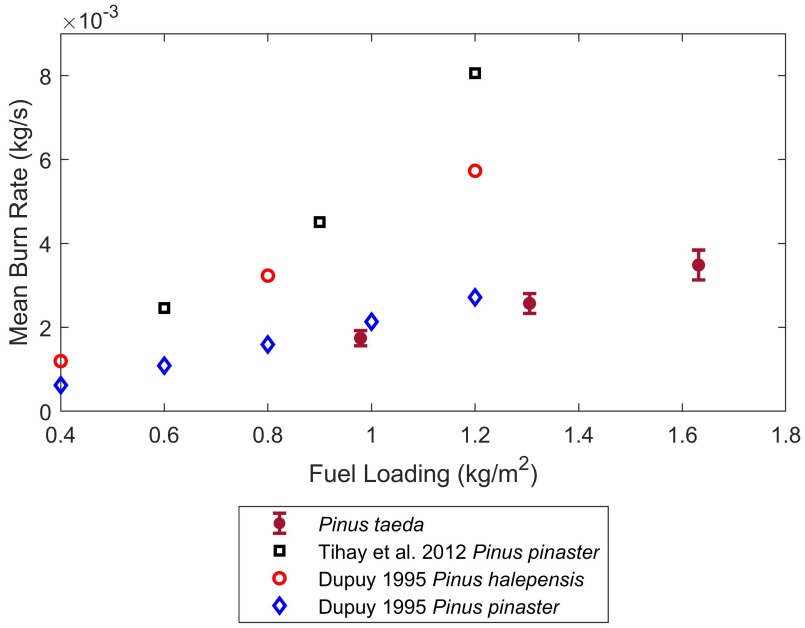

Figure 4.23: Comparison of the mass loss rate measured in the present study to mass loss rate measured from a few similar studies.

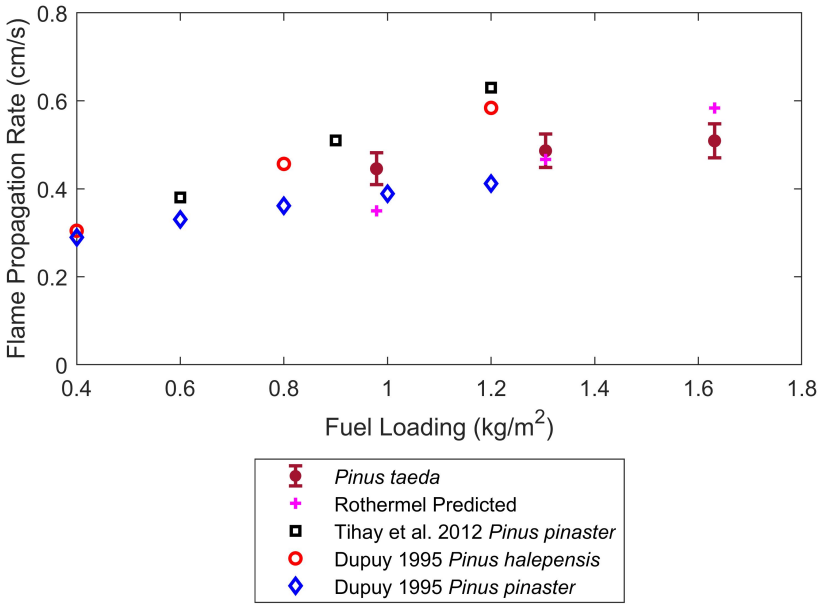

Figure 4.24: Comparison of the flame propagation rate in the present study to flame propagation rate measured from a few similar studies.

The mass loss results shown in Figure 4.23 compare favorably, with the results from the present study appearing most similar to the results from the *P. pinaster* needles studied by Dupuy. This isn't surprising, since the physical characteristics of these fuel beds are most similar. The mass loss rate results presented by Dupuy for the *P. halepensis* fuel beds appear significantly higher than the mass loss rate for both the *P. pinaster* beds measured by Dupuy and the *P. taeda* beds in the current study. This difference is likely due to the higher surface-area to volume ratio and density of the *P. halepensis* needles. The higher surface-area to volume ratio indicates that there is more surface area of the needles for the fire to react with, resulting in more rapid combustion of the needles. Interestingly, the *P. pinaster* needles studied by Tihay et al. show mass loss rates higher than the results from Dupuy suggesting that there is significant variation from study to study. Future work should focus on determining the cause of this variation.

The spread rate results shown in Figure 4.24 also compare favorably. In addition to showing comparison to the Dupuy and Tihay et al. studies, the predicted spread rate from the Rothermel model [23] is also shown. In this case, all spread rates have similar order of magnitude to the rates measured in the present study. Again, the *P. pinaster* beds from the Dupuy are the closest with the results from the Dupuy *P. halepensis* beds and the Tihay et al. *Pinus pinaster* beds having slightly higher propagation results compared to the values measured in the present work. The spread rate predicted by the Rothermel model is of simliar magnitude, but has a strong linear trend not seen in the measured values. This is because the Rothermel model predicts that spread rate will increase as a linear function of fuel loading, which has been called into question by previous works [22].

Overall, the results from the present study compare reasonably well to results from previous similar studies. It might be expected that the results from one type of pine would not be significantly different than the results from another type of pine, but this does not appear to be the case based on the compared results. In fact, even the *P. pinaster* results between the Dupuy and Tihay et al. studies show significant differences despite the beds being comprised of the same fuel and having nearly identical physical properties. The variation in results indicate the need for further

studies to identify the cause of these differences as well as to study the burning characteristics of fuel beds comprised of different fuel types.

Chapter 5

Conclusions

This study has presented valuable insight into the burning characteristics of loblolly pine straw commonly found in the Southeastern United States using an intermediate-scale experimental facility that combines traditional diagnostic techniques with optical methods. Loblolly pine straw was selected due to its prevalence in the Southeastern United States. The specific burning characteristics studied were fuel mass loss rate, fire temperature, fire propagation rate, flame height, flame length, flame surface area, flame intensity, and the pollutant emissions from the fire. Three initial fuel loadings of 0.98, 1.31, and 1.63 $\mathrm{kg/m^2}$ were studied to determine the effect of initial fuel loading on the aforementioned burning characteristics.

The mass loss over time was found to be quasi-steady for all cases. When normalized by initial mass, the normalized mass loss curves were found to have the same slope, indicating a linear relationship between initial fuel loading and mass loss rate. The mean burn rate for each fuel loading was calculated from the mass loss data and it was found that the mean burn rate increased by 2.67E-3 kg/s for every unit increase in fuel loading. The residual mass fraction was found to decrease slightly from 0.23 at a fuel loading of 0.98 $\mathrm{kg/m^2}$ to 0.18 at a fuel loading of 1.63 $\mathrm{kg/m^2}$, indicating an increase in consumption efficiency with fuel loading. The decrease in residual mass fraction is hypothesized to be a result of increased heat output from the fire with increased fuel loading. The increase in heat output was concluded to be a result of increased volume of flame rather than an increase in flame temperature or flame intensity (heat release per unit area).

The temperature of the fire was studied by investigating the maximum temperature seen at locations of 4.45, 14.45, and 24.45 cm above the floor of the facility. The maximum measured temperature was found to decrease throughout the height of the flame. The maximum temperature measured by the bottom row of thermocouples was not found to change significantly, remaining around 980 K, indicating that the temperature in the fuel bed is not affected by fuel loading. Instead fuel bed temperature is likely driven chemical kinetics properties of the pine needles or by a physical property of the needle bed not included in this study such as packing ratio or bulk density. In all cases, flame temperature at the same relative height within the flame did not change much across the different fuel loadings. This suggests that the flame temperature is not affected by the fuel loading, which is not surprising since the fundamental combustion reaction of loblolly pine straw should not be changed by the fuel loading.

The intensity of the flame was calculated from images of the flame taken through a band-pass filter to isolate the CH* radical chemiluminescence wavelength, which effectively isolates the heat release from the light produced by soot and/or hot fuel species. The intensity of the fire was found to not significantly change across the range of fuel loadings tested. This further corroborates the conclusion from the temperature results that the temperature of the fire is primarily driven by the chemical kinetic properties of the actual pine needles rather than the physical arrangement of the fuel bed.

The propagation of the forward-most flame front was tracked optically via the same chemiluminescence images used to calculate the flame intensity. The propagation rate of the fire was found to increase slightly and appear to be approaching an asymptotic maximum across the range of fuel loadings tested. The increase in propagation rate is hypothesized to be a result of the higher heat output from the fires at higher fuel loadings more effectively pre-heating the fuel bed ahead of the flame front. This behavior further corroborates that the increase in burn rate is due to an increase in fuel bed height providing more fuel per unit length of the fuel bed for the fire to consume rather than from an increase in the spread rate of the fire. The mass loss rate was calculated from the propagation rate data with the assumption that all mass consumption was from an infinitely thin

flame propagating along the length of the fuel bed. This calculated mass loss rate was compared with the actual measured mass loss rate and these values were found to be in good agreement. This indicates that the majority of the mass loss rate was, in fact, coming from the flaming combustion rather than secondary or smoldering combustion. The mass loss rate calculated from the propagation rate was found to increasingly overestimate the actual mass loss rate as fuel loading was increased, this was taken to indicate that increasing amounts of secondary and smoldering combustion were occurring behind the primary flame front as fuel loading increased.

The CH* chemiluminescence images were also used to measure the height of the flame relative to the fuel bed. The flame height was found to increase asymptotically across the range of fuel loadings tested. Since the flame height was measured from the CH* intensity images, the measured flame height represents the height of the actual combusting region of the flame. The increase in flame height with fuel loading was hypothesized to result from the increase in fuel available for burning per unit length of the fuel bed.

The length of the flame was investigated as well and was found to increase both with fuel loading and throughout the duration of the burns. The increase with fuel loading was taken to be a result of the increased fuel bed height resulting in secondary flaming and smoldering combustion continuing behind the flame front to consume through the height of the fuel bed. The increase in flame width throughout the test was taken to indicate that the primary flame front is propagating faster than the regions of secondary combustion, which indicates that the regions of secondary combustion are not consuming fuel as quickly as the primary flame front.

The flame surface area was measured and was found to increase with a near linear relationship to fuel loading, not exhibiting the same asymptotic decay as was seen with the increase in flame height. As such, it was concluded that the increase flame length was contributing to the increase in flame surface area in such a way that removed the asymptotic effects of the flame height. Since the propagation rate remains nearly constant, and the mass consumption rate increases with fuel loading, it logically follows that more fuel is being combusted at any moment in time with the higher fuel loading fires. Since the flame temperature and intensity per unit area of the flame were

not found to change significantly with fuel loading, the increase in fuel consumption rate was taken to be a result of an increase in the overall size (volume) of the fire, which is corroborated by the flame surface area measurements. This increase in the total size of the fire results in more heat being output, which was attributed to the decrease in residual mass fraction seen with increasing fuel loading.

The emissions data was analyzed to study the effect that fuel loading had on the CO, NOx, and SO_2 emissions of a loblolly pine straw fire. Carbon monoxide emissions were found to increase significantly with fuel loading while SO_2 increased only slightly and NOx remained at nearly zero. This result is not surprising since the relatively low temperatures associated with wildland fires result in incomplete combustion, which produces CO, and are not high enough to support the nitrogen and oxygen reactions required for the production of NOx.

The results presented here provide a better understanding of how fire spreads through a loblolly pine straw bed. This information can be used to improve prescribed burning practices used to reduce the risk of uncontrolled fire and manage ecosystem health. Perhaps the most useful case for the data presented here is in validating and improving many of the wildland fire modeling and simulation codes under development such as the Fire Dynamics Simulator (FDS) published by the National Institute of Standards and Technology [43]. Other modeling codes such as FARSITE [44], BehavePlus [45], and FlamMap [46] stand to benefit as well. In particular, there exists a need for data on specific types of fuel in order to adequately develop fire spread models through different fuels and ensure that those models are properly validated. The data provided here can be used to assess the performance of the existing fuel models by way of numerically simulating the experimental facility used. The multiple burning characteristics all measured simultaneously in real-time throughout the duration of the burn provide multiple points of comparison to the results from the numerical simulations yielding a more robust validation compared to simply validating the rate of spread and/or mass loss rate. In the future, the developed facility can be used to study different wildland fuels, fuel mixtures, and physical properties of the fuel bed such as packing ratio, bulk density, fuel moisture content, and slope. While beyond the scope of this present study,

these future works would contribute even more valuable validation data for modeling codes under development.

References

[1] A. Carr, "Gatlinburg Residents Get First Look at Destruction Left Behind By Wildfire," 2013.

[2] "California Statewide Fire Summary," 2017.

[3] D. Kasler, "Wine country wildfire costs now top $9 billion, costliest in California history," 2017.

[4] "Thousands evacuated after wildfire on France's Mediterranean cost," 2017.

[5] A. Susaeta and P. Gong, "Economic viability of longleaf pine management in the Southeastern United States," *Forest Policy and Economics*, vol. 100, no. November 2018, pp. 14–23, 2019.

[6] S. E. McKeand, "The evolution of a seedling market for genetically improved loblolly pine in the southern United States," *Journal of Forestry*, vol. 117, no. 3, pp. 293–301, 2019.

[7] R. P. Guyette, M. C. Stambaugh, D. C. Dey, and R. M. Muzika, "Predicting Fire Frequency with Chemistry and Climate," *Ecosystems*, vol. 15, no. 2, pp. 322–335, 2012.

[8] T. Elder, J. S. Kush, and S. M. Hermann, "Thermogravimetric analysis of forest understory grasses," *Thermochimica Acta*, vol. 512, no. 1, pp. 170–177, 2011.

[9] V. Leroy, D. Cancellieri, and E. Leoni, "Thermal degradation of ligno-cellulosic fuels: DSC and TGA studies," *Thermochimica Acta*, vol. 451, no. 1-2, pp. 131–138, 2006.

[10] P. Rovira, C. Kurz-Besson, M. M. Coûteaux, and V. Ramón Vallejo, "Changes in litter properties during decomposition: A study by differential thermogravimetry and scanning calorimetry," *Soil Biology and Biochemistry*, vol. 40, no. 1, pp. 172–185, 2008.

[11] E. Amini, M. S. Safdari, D. R. Weise, and T. H. Fletcher, "Pyrolysis kinetics of live and dead wildland vegetation from the Southern United States," *Journal of Analytical and Applied Pyrolysis*, vol. 142, no. April, p. 104613, 2019.

[12] M. B. Dickinson, T. F. Hutchinson, M. Dietenberger, F. Matt, and M. P. Peters, "Litter species composition and topographic effects on fuels and modeled fire behavior in an oak-hickory forest in the Eastern USA," *PLoS ONE*, 2016.

[13] R. H. White, D. R. Weise, K. Mackes, and A. C. Dibble, "Cone calorimeter testing of vegetation–an update," *International conference on fire safety*, vol. 35, no. Astm 1999, pp. 1–13, 2002.

[14] L. D. Prior, B. P. Murphy, G. J. Williamson, M. A. Cochrane, W. M. Jolly, and D. M. Bowman, "Does inherent flammability of grass and litter fuels contribute to continental patterns of landscape fire activity?," *Journal of Biogeography*, 2017.

[15] R. W. Fonda, "Needles from Eight Pine Species," *Forest Science*, vol. 47, no. 3, pp. 390–396, 2001.

[16] T. Barboni, F. Morandini, L. Rossi, T. Molinier, and P. A. Santoni, "Relationship between flame length and fireline intensity obtained by calorimetry at laboratory scale," *Combustion Science and Technology*, vol. 184, no. 2, pp. 186–204, 2012.

[17] F. Morandini, A. Simeoni, P. A. Santoni, and J. H. Balbi, "A model for the spread of fire across a fuel bed incorporating the effects of wind and slope," *Combustion Science and Technology*, vol. 177, no. 7, pp. 1381–1418, 2005.

[18] P.-A. Santoni, F. Morandini, and T. Barboni, "Steady and unsteady fireline intensity of spreading fires at laboratory scale," *The Open Thermodynamics Journal*, vol. 4, no. 1, 2010.

[19] F. Morandini, Y. Perez-Ramirez, V. Tihay, P. A. Santoni, and T. Barboni, "Radiant, convective and heat release characterization of vegetation fire," *International Journal of Thermal Sciences*, vol. 70, pp. 83–91, 2013.

[20] V. Tihay, F. Morandini, P. A. Santoni, Y. Perez-Ramirez, and T. Barboni, "Study of the influence of fuel load and slope on a fire spreading across a bed of pine needles by using oxygen consumption calorimetry," *Journal of Physics: Conference Series*, vol. 395, p. 012075, 2012.

[21] F. Morandini, X. Silvani, D. Honoré, G. Boutin, A. Susset, and R. Vernet, "Slope effects on the fluid dynamics of a fire spreading across a fuel bed: PIV measurements and OH chemiluminescence imaging," *Experiments in Fluids*, 2014.

[22] J. L. Dupuy, "Slope and fuel load effects on fire behaviour :Laboratory experiments in pine needles fuel beds," *International Journal of Wildland Fire*, vol. 5, no. 3, pp. 153–164, 1995.

[23] R. C. Rothermel, "A mathematical model for predicting fire spread in wildland fuels," tech. rep., USDA Forest Service, 1972.

[24] J. L. Dupuy, J. Maréchal, D. Portier, and J. C. Valette, "The effects of slope and fuel bed width on laboratory fire behaviour," *International Journal of Wildland Fire*, vol. 20, no. 2, pp. 272–288, 2011.

[25] X. Silvani, F. Morandini, and J. L. Dupuy, "Effects of slope on fire spread observed through video images and multiple-point thermal measurements," *Experimental Thermal and Fluid Science*, vol. 41, pp. 99–111, 2012.

[26] Y. Wu, H. J. Xing, and G. Atkinson, "Interaction of fire plume with inclined surface," *Fire Safety Journal*, vol. 35, no. 4, pp. 391–403, 2000.

[27] F. Morandini, X. Silvani, and A. Susset, "Feasibility of particle image velocimetry in vegetative fire spread experiments," *Experiments in Fluids*, vol. 53, no. 1, pp. 237–244, 2012.

[28] J. Lozano, W. Tachajapong, D. R. Weise, S. Mahalingam, and M. Princevac, "Fluid dynamic structures in a fire environment observed in laboratory-scale experiments," *Combustion Science and Technology*, vol. 182, no. 7, pp. 858–878, 2010.

[29] F. Morandini, X. Silvani, J. L. Dupuy, and A. Susset, "Fire spread across a sloping fuel bed: Flame dynamics and heat transfers," *Combustion and Flame*, vol. 190, pp. 158–170, 2018.

[30] V. Tihay, F. Morandini, P.-A. Santoni, Y. Perez-Ramirez, and T. Barboni, "Combustion of forest litters under slope conditions: Burning rate, heat release rate, convective and radiant fractions for different loads," *Combustion and Flame*, vol. 161, no. 12, pp. 3237 – 3248, 2014.

[31] P. A. Santoni, F. Morandini, and T. Barboni, "Determination of fireline intensity by oxygen consumption calorimetry," *Journal of Thermal Analysis and Calorimetry*, vol. 104, no. 3, pp. 1005–1015, 2011.

[32] X. Zhou, S. Mahalingam, and D. Weise, "Experimental study and large eddy simulation of effect of terrain slope on marginal burning in shrub fuel beds," *Proceedings of the Combustion Institute*, vol. 31 II, pp. 2547–2555, 2007.

[33] D. R. Weise, E. Koo, X. Zhou, S. Mahalingam, F. Morandini, and J. H. Balbi, "Fire spread in chaparral - A comparison of laboratory data and model predictions in burning live fuels," *International Journal of Wildland Fire*, vol. 25, no. 9, pp. 980–994, 2016.

[34] W. R. Catchpole, E. A. Catchpole, B. W. Butler, R. C. Rothermel, G. A. Morris, and D. J. Latham, "Rate of spread of free-burning fires in woody fuels in a wind tunnel," *Combustion Science and Technology*, vol. 131, no. 1-6, pp. 1–37, 1998.

[35] J. M. Mendes-Lopes, J. M. Ventura, and J. M. Amaral, "Flame characteristics, temperature-time curves, and rate of spread in fires propagating in a bed of Pinus pinaster needles," *International Journal of Wildland Fire*, vol. 12, no. 1, pp. 67–84, 2003.

[36] W. R. Anderson, E. A. Catchpole, and B. W. Butler, "Convective heat transfer in fire spread through fine fuel beds," *International Journal of Wildland Fire*, vol. 19, no. 3, pp. 284–298, 2010.

[37] F. Morandini, X. Silvani, L. Rossi, P. A. Santoni, A. Simeoni, J. H. Balbi, J. Louis Rossi, and T. Marcelli, "Fire spread experiment across Mediterranean shrub: Influence of wind on flame front properties," *Fire Safety Journal*, 2006.

[38] G. M. Davies and C. J. Legg, "Fuel Moisture Thresholds in the Flammability of Calluna vulgaris," *Fire Technology*, vol. 47, no. 2, pp. 421–436, 2011.

[39] C. Awad, D. Morvan, J.-L. Rossi, T. Marcelli, F. J. Chatelon, F. Morandini, and J.-H. Balbi, "Fuel moisture content threshold leading to fire extinction under marginal conditions," *Fire Safety Journal*, vol. 118, p. 103226, 2020.

[40] J. Ballester and T. García-Armingol, "Diagnostic techniques for the monitoring and control of practical flames," *Progress in Energy and Combustion Science*, vol. 36, no. 4, pp. 375–411, 2010.

[41] S. Sardeshmukh, M. Bedard, and W. Anderson, "The use of oh* and ch* as heat release markers in combustion dynamics," *International Journal of Spray and Combustion Dynamics*, vol. 9, no. 4, pp. 409–423, 2017.

[42] S. Turns, *An Introduction to Combustion: Concepts and Applications*. McGraw-Hill series in mechanical engineering, McGraw-Hill, 2012.

[43] K. McGrattan, S. Hostikka, R. McDermott, J. Floyd, C. Weinschenk, and K. Overholt, "Fire Dynamics Simulator User's Guide," tech. rep., 2013.

[44] U. F. Service, “FARSITE,” 2018.

[45] P. L. Andrews, “Current status and future needs of the BehavePlus Fire Modeling System,” *International Journal of Wildland Fire*, vol. 23, no. 1, pp. 21–33, 2014.

[46] M. A. Finney, “An overview of flammap fire modeling capabilities,” in *In: Andrews, Patricia L.; Butler, Bret W., comps. 2006. Fuels Management-How to Measure Success: Conference Proceedings. 28-30 March 2006; Portland, OR. Proceedings RMRS-P-41. Fort Collins, CO: US Department of Agriculture, Forest Service, Rocky Mountain Research Station. p. 213-220*, vol. 41, 2006.